Chapter 6

Results and Discussion

This chapter is organized in the same fashion as the theory; first, the quantum chemical investigations will be presented; second, the quantum dynamical simulations will be discussed with respect to the theoretical absorption spectra; third, quantum control will be achieved in the time domain with a pump-dump type control mechanism; and last, the chapter will end with results from the application of OCT to NMT.

6.1   Quantum Chemistry

The *ab initio* calculations for two organometallic complexes are presented and compared here. The first complex is the tetracarbonylhydridocobalt complex, $HCo(CO)_4$, for which the corresponding electronic energies and surfaces were calculated in the work group of Daniel *et al.* (Strasbourg), the second molecule is the tetracarbonylmethylcobalt complex, $CH_3Co(CO)_4$, and its quantum chemical investigation has been done in Berlin. This section is divided up into three subsections. The first subsection will concentrate on the structure and electronic spectra, the second subsection on the state correlation diagrams and the 2-dimensional potential energy surfaces, and the final subsection will focus on the eigenvalues and eigenfunctions for both complexes. Each section is further partitioned into computational details (they differ for each subsection) and results.

6.1.1 Model

The two organometallic molecules, $HCo(CO)_4$ and $CH_3Co(CO)_4$, can be viewed generally in an idealized form as given in fig. 6.1, where the hydrogen and methyl groups are denoted by R, i.e. R=H,CH_3. The remaining ligands are all carbonyl groups, one of which sits at an axial position along with the R group, while the other three are located along the equatorial positions, slightly angled away from the axial carbonyl. The structure of the complex is distorted trigonal bipyramidal and belongs to the C_{3v} symmetry point group. The principle C_3 axis, which describes the threefold order of rotation that results in equivalent representations of the molecule, is oriented along the z-axis, see fig. 6.1. The two degrees of freedom that are investigated in this work are the bond lengths of the axial ligands, Co-R (R=H and CH_3) and Co-CO_{ax}, and will be referred to generally as q_1 and q_2 respectively. Under such considerations, the complexes can be considered as pseudo-triatomic molecules.

Figure 6.1: The idealized structure of $RCo(CO)_4$ (R=H,CH_3) is categorized under the C_{3v} point group in which the z-axis is the principle axis, and has a distorted trigonal bipyramidal geometry.
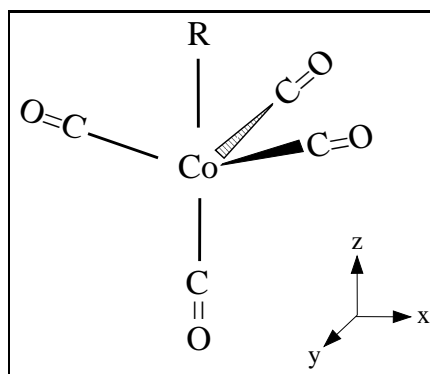
The electronic configuration of $RCo(CO)_4$ (R=H, CH_3) in its $^1A_1$ ground state is described by the following orbital occupancies $(\sigma_{Co-R})^2(3d_\pi)^4(3d_\delta)^4$, the σ_{Co-R} bonding orbital being of a_1 symmetry and the $3d_\pi$ (d_{xz},d_{yz}) and d_δ ($d_{x^2-y^2}$,d_{xy}) of e symmetry. The low-lying vacant orbitals correspond to the σ^*_{Co-R} and π^*_{CO} antibonding orbitals.

6.1.2 DFT Geometry Optimization and Electronic Spectra

The geometry optimization for $HCo(CO)_4$ and $CH_3Co(CO)_4$ are carried out using density functional theory (DFT) and the electronic transition energies are calculated using time-dependent DFT (TD-DFT) and CASSCF/MS-CASPT2 methods, see sections 2.2.3 and

2.2.4. The geometry optimization for both complexes needed to be performed because the experimental geometry of the methyl complex is not available. Ensuing calculations for $CH_3Co(CO)_4$ are initiated from the DFT optimized geometry. The electronic transition energies for the hydrido complex were investigated using both the experimental [131] as well as the DFT optimized geometries.

Computational Details

The electronic calculations for the $RCo(CO)_4$ (R=H,CH_3) organometallic complexes have been performed using C_s symmetry under the C_{3v} constraint. Two methods were applied for the comparison of the electronic energies: TD-DFT and CASSCF/MS-CASPT2. The computational details are given below for both.

TD-DFT The TD-DFT calculations have been performed using GAUSSIAN 03 software [132] using the B3LYP functional [133, 134] with the 6-31G(d) basis sets for all atoms [135]. In order to validate the use of the DFT optimized geometry for $CH_3Co(CO)_4$, the TD-DFT calculations have been performed using the DFT optimized geometry for both molecules as well as for the experimental structure of $HCo(CO)_4$.

CASSCF/MS-CASPT2 In order to describe the electronic spectroscopy, more accurately multiconfigurational calculations have been performed. The CASSCF active space must include the 3d occupied orbitals of the Co, the bonding and antibonding sigma orbitals, σ and σ^*, localized on the Co-R sigma bond and some of the low-lying carbonyl antibonding pi orbitals, π^*_{CO}. Additional orbitals also have to be included in the active space to assure a good description of non-dynamical correlation effects. Electronic calculations for the hydride complex have included 16 active electrons correlated into 13 active orbitals whereas for the methyl complex 16 active electrons have been correlated into 14 active orbitals. The following atomic natural orbitals (ANO-Small) basis sets [136] have been used for both complexes: a (17s, 12p, 9d, 4f) contracted to [6s, 4p, 3d, 2f] for the cobalt atom, a (10s, 6p, 3d) contracted to [3s, 2p, 1d] for the carbon and oxygen atoms and a (7s, 3p) contracted to [2s, 1p] for the hydrogen atom. The additional dynamical electronic correlation effects have been taken into account by means of MS-CASPT2 calculations with level shifts [137] of 0.3-0.4 a.u. in order to avoid intruder states. The

CASSCF/MS-CASPT2 calculations have been performed with the MOLCAS 6.0 package [138].

The oscillator strengths, f, have been calculated using the CAS wave functions and the MS-CASPT2 energy. Because the calculations have been carried out in C_s symmetry, a subgroup of C_{3v}, the degenerate states of $^1A'$ and $^1A''$ symmetry that compose the ^1E states are paired and the excitation energies and oscillator strengths are averaged for each pair. A set of 8 roots averaged for the A' symmetry and 9 averaged states for the $^1A''$ symmetry have been used for both complexes in the CASSCF and MS-CASPT2 calculations. The number of roots chosen were based off of the lowest 8 A' states which consequently included 9 A'' states.

Results

Geometry Optimization   The most important geometrical parameters of the two complexes optimized with DFT together with the available experimental values are shown in fig. 6.2. The comparison between the experimental and the DFT optimized structures of $HCo(CO)_4$ (cf. fig. 6.2) gives a reasonable agreement for the Co-H bond distance (1.556 Å vs. 1.494 Å) and the bond angles $HCoC_{eq}$ (80.3° vs. 81°) and $C_{ax}CoC_{eq}$ (99.7° vs. 99.0°). The optimized values of 1.812 Å for the Co-C_{ax} bond and of 1.801 Å for the Co-C_{eq} bond show an overestimate with respect to the experimental values for the Co-CO axial bond length (1.764 Å) and an underestimate of the Co-CO equatorial bond (1.818 Å). This behavior has also been reported for a number of transition metal carbonyls [139, 140]. The O-C-Co angle has been considered to be 180° for all carbonyls.

For the methyl substituted complex on the right of fig. 6.2 the metal-carbonyl bonds have been calculated at 1.806 Å (Co-C_{eq}) and 1.812 Å (Co-C_{ax}). Comparison of these geometrical results agree rather well with those published by Ziegler *et al.* using DFT (LDA) calculations [139, 140]. The optimized Co-CH_3 bond distance in this study is 2.086 Å, in agreement with the calculated value of 2.080 Å by Ziegler *et al.* The difference in bond length between the Co-CH_3 and the Co-H bonds is calculated at 0.592 Å, and is also consistent with the difference found for $RCo(CO)_4$ (0.609 Å) and $RMn(CO)_5$ (0.611 Å) [139, 140]. The $C_{ax}CoC_{eq}$ bond angle with a value of 96.19° is larger than the opposed value of 94.4°. Lastly, the calculated angle of the pseudo-linear Co-CO fragment is 176.2°, and is comparable with the value of 178.7° computed by Ziegler *et al.*
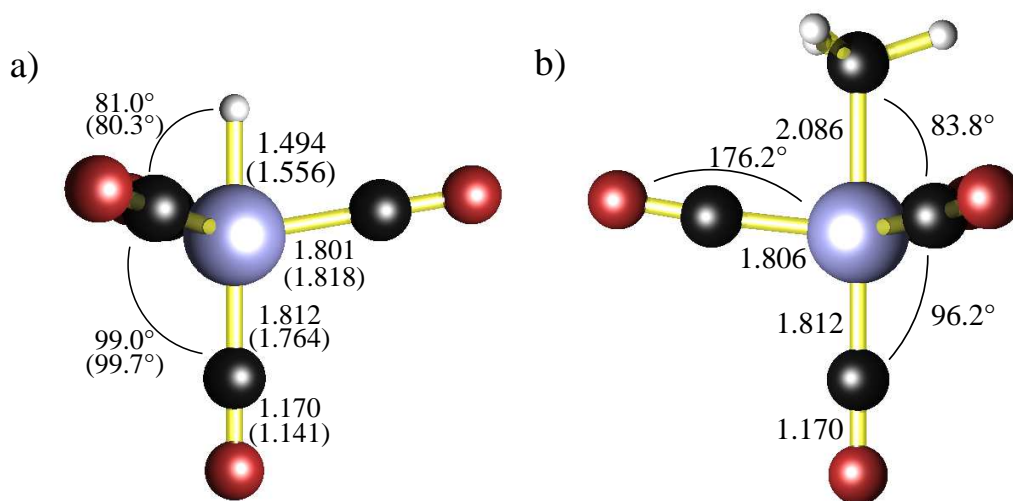
Figure 6.2: The most relevant geometrical parameters for a) $HCo(CO)_4$ and b) $CH_3Co(CO)_4$ optimized at B3LYP level of theory where distances are measured in angstroms Å and the angles in degrees °. The values in parenthesis correspond to the experimental structure [131].

The main difference between the two substituted complexes, $RCo(CO)_4$ (R=H, CH_3), is the metal-R bond distance which is, as expected, much shorter in the hydrido complex. Besides the larger size of the alkyl ligand, the longer bond length is related to the weakening of metal-alkyl bonds by a two-orbital, four-electron repulsive interaction which can not occur in the hydride complex [139]. Its consequence on the absorption spectrum will be the occurrence of electronic transitions corresponding to $\sigma_{Co-CH_3} \rightarrow \pi_{CO}^*$ excitations in the far-UV domain of energy which are not present in the spectrum of $HCo(CO)_4$.

Electronic Transition Energies   The MS-CASPT2 and TD-DFT transition energies from the ground state a^1A_1 to the first six low-lying states of $HCo(CO)_4$ and $CH_3Co(CO)_4$ complexes are reported in table 6.1 together with their associated oscillator strengths, f. The MS-CASPT2 transition energies for both complexes are reported only for the DFT optimized geometry. The TD-DFT transition energies and oscillator strengths are reported for the experimental structure as well as for the optimized DFT geometry for $HCo(CO)_4$, however for $CH_3Co(CO)_4$ the TD-DFT excited state calculations have been performed only on the DFT optimized geometry.

Three types of electronic transitions describe the first six excited electronic states. The first type, corresponding to the first two lowest lying excited states for both complexes

(a^1E and b^1E), is defined by a Metal-to-Sigma-Bond-Charge-Transfer (MSBCT). This electronic transition occurs from the cobalt metal to the sigma bonds of the hydride or the methyl ligand. The second type is known as the Metal-to-Ligand-Charge-Transfer (MLCT) and corresponds to an electronic transition from the metal d-orbitals to a π^* orbital of the ligand. This type of transition describes the c^1E, b^1A_1, d^1E and e^1E states for the hydrido complex and the c^1E, b^1A_1, d^1E for the methyl complex. The last transition is a Sigma-Bond-to-Ligand-Charge-Transfer (SBLCT) and describes the e^1E state for the methyl complex.

The experimental information on the electronic spectroscopy of this class of transition metal carbonyls is scarce. Both complexes absorb at 254 nm (or 39370 cm^{-1}) [141, 142, 143] and the band for $HCo(CO)_4$ starts at 34000 cm^{-1}. The absorption spectrum of this hydrido complex is characterized by an intense band at 44000 cm^{-1} [142, 143]. The absorption spectra of the hydrido and methyl complexes calculated here are very similar with lowest energy absorption occurring at ca. 35000 cm^{-1} and 34000 cm^{-1}, respectively. The four low-lying states calculated between 35740 cm^{-1} and 42040 cm^{-1} for $HCo(CO)_4$ and 33980 cm^{-1} and 42340 cm^{-1} for $CH_3Co(CO)_4$ should each contribute to its own band with the maximum of each centered around its transition energy, given in table 6.1. According to the calculated oscillator strengths, the MLCT states are the major contributors. The far-UV domain of the spectrum is characterized by strong absorption bands corresponding to the two ^1E MLCT states (d^1E and e^1E). The d^1E of $HCo(CO)_4$ with an oscillator strength of 0.08 should be responsible for the intense band observed at 44000 cm^{-1} [142, 143]. This band is shifted to higher energies in the methyl derivative at 48000 cm^{-1}. The $CH_3Co(CO)_4$ compound should produce another peak of intermediate strength at ca. 50000 cm^{-1} corresponding to a MSBCT state ($\sigma_{Co-Me} \rightarrow \pi^*_{CO}$), while in the hydride analogue the MSBCT state is replaced by a MLCT state appearing at lower energies (48000 cm^{-1}).

The TD-DFT excitation energies and oscillator strengths obtained for the experimental and DFT optimized geometries for $HCo(CO)_4$ agree rather well, validating the use of DFT in the obtention of geometries for these complexes. However, the assignment of the states in the TD-DFT calculation for both complexes differ significantly from the *ab initio* values and the relative positions of the b^1E and the c^1E / b^1A_1 MLCT states are modified, see table 6.1. TD-DFT calculations indicate an intercalation of one and two MLCT states between the lowest MSBCT states in the electronic spectra of $CH_3Co(CO)_4$ and $HCo(CO)_4$, respectively. A comparison of the TD-DFT transition energies with the

State	Main Configuration	MS-CASPT2		TD-DFT[a]		TD-DFT[b]	
		ΔE	f	ΔE	f	ΔE	f
R=H							
$a^1A_1 \rightarrow a^1E$	$3d_\delta \rightarrow \sigma^*_{\text{Co}-\text{R}}$	35740	0.001	30560	≈ 0.0	30860	≈ 0.0
$a^1A_1 \rightarrow b^1E$	$3d_\pi \rightarrow \sigma^*_{\text{Co}-\text{R}}$	40280	0.001	36900	0.002	37580	0.001
$a^1A_1 \rightarrow c^1E$	$3d_\delta \rightarrow \pi^*_{\text{CO}}$	41320	0.040	34400	0.002	35150	0.006
$a^1A_1 \rightarrow b^1A_1$	$3d_\delta \rightarrow \pi^*_{\text{CO}}$	42040	0.080	35900	0.028	36410	0.023
$a^1A_1 \rightarrow d^1E$	$3d_\delta \rightarrow \pi^*_{\text{CO}}$	44190	0.080	38100	0.033	38945	0.036
$a^1A_1 \rightarrow e^1E$	$3d_\pi \rightarrow \pi^*_{\text{CO}}$	49900	0.040			43280	< 0.001
R=CH$_3$							
$a^1A_1 \rightarrow a^1E$	$3d_\delta \rightarrow \sigma^*_{\text{Co}-\text{R}}$	33980	0.002	29345	0.001		
$a^1A_1 \rightarrow b^1E$	$3d_\pi \rightarrow \sigma^*_{\text{Co}-\text{R}}$	38390	0.003	34650	0.001		
$a^1A_1 \rightarrow c^1E$	$3d_\delta \rightarrow \pi^*_{\text{CO}}$	40720	0.018	33120	0.003		
$a^1A_1 \rightarrow b^1A_1$	$3d_\delta \rightarrow \pi^*_{\text{CO}}$	42340	0.014	34740	0.016		
$a^1A_1 \rightarrow d^1E$	$3d_\pi \rightarrow \pi^*_{\text{CO}}$	48200	0.036	37790	0.024		
$a^1A_1 \rightarrow e^1E$	$\sigma_{\text{Co}-\text{Me}} \rightarrow \pi^*_{\text{CO}}$	52290	0.020	45750	0.068		

[a] TD-DFT performed on the DFT optimized structure of HCo(CO)$_4$

[b] TD-DFT performed on the experimental structure of HCo(CO)$_4$

Table 6.1: CASSCF/MS-CASPT2 and TD-DFT transition energies ΔE, given in h·c·cm^{-1}, for the low-lying electronic states of RCo(CO)$_4$ (R=H,CH$_3$) and associated oscillator strengths f.

ab initio values show a discrepancy of more than 0.5 eV for nearly all transitions. The TD-DFT values are underestimated in comparison. This discrepancy could be due to the use of a standard B3LYP functional which may treat the MLCT and MSBCT states differently. This underestimation of TD-DFT transition energies has been observed in a number of transition metal complexes [144].

6.1.3 State Correlation Diagrams and 2-D PES

Computational Details

The calculations for the state correlation diagrams and the 2-D PESs have been performed using the multiconfigurational CASSCF method [145] and MS-CASPT2 [63], see section 2.2.3, with the MOLCAS 6.0 package [138]. Calculations for both complexes were car-

ried out using the same basis set as in section 6.1.2. The CASSCF correlation diagrams have been calculated for both complexes using an active space of 10 electrons correlated in 14 active orbitals CAS(10,14) by means of a state-average approach including 9(A') and 8(A'') states for $HCo(CO)_4$ and 5(A') and 4(A'') states for $CH_3Co(CO)_4$. Three occupied orbitals were removed from the active space (two from A' and one from the A'' symmetry) and correspond to orbitals associated to bonding within the ligand. Consequently, these orbitals have little significance in describing the bonding to the metal atom, and their removal decreases the computational time. Also, we have focused our attention to the four low-lying transitions of the methyl complex. The values at the asymptotic limits are obtained with the corresponding R or CO_{ax} ligands positioned at 50 Å while the rest of the geometry is kept frozen at the equilibrium. A level shift of 0.3 E_h has been used in the MS-CASPT2 calculations to get rid of the dramatic problem of intruder states. The same non-relaxed approach is followed in calculating the PES at the CASSCF level along the internuclear coordinates, q_1 and q_2, defined as the bond distance of d(Co-R) and d(Co-CO_{ax}), respectively. This approach is justified because the direct dissociation of the ligands R and CO will typically take place in less than 100 femtoseconds (fs) and within this time scale the rest of the molecule should not have time to relax.

The relevant potential energy surfaces were calculated using a set of five (5) equally averaged states for the $^1A'$ symmetry, by employing a CAS (10,14) and CAS (10,12) space for R=H, CH_3 complexes, respectively. The number of active orbitals for the methyl complex were again diminished by two. This decision is based on the correlation diagrams, in which only three and four states could be correlated for the A' and A'' symmetry, see fig. 6.3. The removal of the two orbitals have little effect in the calculation of the potential energy surfaces and are removed for computational convenience. Since A' and A'' states are degenerate, only the A' symmetry has been considered. The potential functions used in the wavepacket propagations were constructed by a spline fit technique using over 150 *ab initio* points. The upper two bound states, c^1E and b^1A_1 for $CH_3Co(CO)_4$ have been successfully calculated from 1.78 to 2.69 Å and from 1.71 to 2.41 Å for q_1 and q_2, respectively. At longer bond lengths these states get crossed by other states and increase rapidly to higher energies, as evidenced from the state correlation diagrams which were calculated with inclusion of more states. In order to prevent possible dissociation along the Co-CO bond the c^1E and b^1A_1 states, the PESs were extended 0.4 Å. The remainder of the grid was extended with the final energy value of the calculated state, creating an upper plateau, to match the grid size of the three lower lying states. These three states were calculated from 1.48 to 50.0 Å and from 1.21 to 50.0 Å for the coordinates q_1 and q_2 respectively.

Results

Bond Dissociation Energies   The bond dissociation energies were calculated from the data accrued from the construction of the state correlation diagrams. These energies were calculated at the CASSCF and MS-CASPT2 levels of theory for $HCo(CO)_4$ and $CH_3Co(CO)_4$ are reported in table 6.2 together with the experimental data when available [146] and other theoretical values [139, 147]. The calculated CASSCF and MS-CASPT2 Co-CO_{ax} bond dissociation energies for the hydrido complex are 37.9 and 65.8 kcal/mol respectively and 20.0 and 55.2 kcal/mol for the methyl complex. These values can be compared to both experimental and theoretical values for $Fe(CO)_5$, $Ni(CO)_4$ and $Cr(CO)_6$, which lie in the range 39.0-44.2 kcal/mol, 25.0-29.8 kcal/mol and 32.7-42.7 kcal/mol [147], respectively.

The CASSCF dissociation energies are in surprisingly good agreement with the experimental and other theoretical studies using DFT. Multistate CASPT2 calculations fail to correctly reproduce the experimental values for the Co-R (R=H, CH_3) bond as well as for the Co-CO_{ax} bond dissociation energies, which are systematically overestimated on the order of 20.0-30.0 kcal/mol. This effect is more significant for the Co-CO_{ax} bond than for the Co-R (R=H, CH_3) bond. This is a consequence of the unbalanced description between the equilibrium and asymptotic electronic structures by means of perturbation theory incorporating a level shift technique and based on a rather limited CASSCF zero-order wave function. Indeed the $^1A_1$ electronic ground state at equilibrium seems to be over stabilized with respect to the asymptotes when going from the CASSCF to the MS-CASPT2 (31 kcal/mol for instance for $CH_3Co(CO)_4$). A tentative explanation is based on the reduced active space used to build the zero-order wave function. Only the occupied $3d_{Co}$ and σ_{Co-R} orbitals (bonding combination of the $d_{z^2}(Co)$ with the s(H) (R=H) or sp(C) (R=CH_3) orbitals) and their unoccupied counterparts belong to the active space. In particular, while a correct description of the Co-R sigma interaction is warranted at the equilibrium structure by the presence of the σ_{Co-R} and σ^*_{Co-R} orbitals in the active space this is not the case at the asymptote. Indeed, the absence of the σ_{CO} orbital in the active space prevents the necessary sp/d_{z^2} hybridization that stabilizes the unsaturated fragment $RCo(CO)_3$ at dissociation via an enhanced Co-R sigma bonding interaction. This is illustrated by a destabilization of the σ_{CO} orbital due to an underestimation of this interaction and by a decrease of the occupation of the corresponding CASPT2 natural orbitals, from 1.92 to 1.90 for $HCo(CO)_4$ and from 1.88 to 1.81 for $CH_3Co(CO)_4$, when moving from

	CASSCF	MS-CASPT2	Experimental[a]	Other[b]
$HCo(CO)_4$				
Co-H	62.2	76.6	57.0	55.0
$Co-CO_{ax}$	37.9	65.8	-	-
$CH_3Co(CO)_4$				
$Co-CH_3$	37.0	60.6	-	38.27
$Co-CO_{ax}$	20.0	55.2	-	-

[a] Taken from ref. [146].

[b] Taken from ref. [139].

Table 6.2: CASSCF and MS-CASPT2 Co-R (R=H, CH_3) and $Co-CO_{ax}$ bond dissociation energies given in kcal/mol for $HCo(CO)_4$ and $CH_3Co(CO)_4$ compared to the available experimental and other theoretical values.

the equilibrium structure to the asymptote. A similar effect is observed when calculations of the elongated Co-R bond are performed to produce $CO_{ax}Co(CO)_3$. However, since the CO ligand is less of a sigma donor than H or CH_3, this effect is attenuated and the error on bond dissociation energy falls from 25.0 - 30.0 kcal/mol for the $Co-CO_{ax}$ bond dissociation energy to 20.0 - 22.0 kcal/mol for the Co-R bonds. Since the poor values for the dissociation energy at the MS-CASPT2 level are due to the destabilization of the unsaturated fragment, the only way to rectify the calculation would be to use a huge active space combined with full geometry optimization of both the reactants and primary products at the same level of theory, which is computationally inhibited. Therefore, the state correlation diagrams and the PES presented in the next section have been built at the CASSCF level and should be adequate to draw a qualitative picture of a direct ultrafast deactivation mechanism after UV absorption for both of the complexes.

State Correlation Diagrams   The CASSCF energies for the a^1A_1 electronic ground state, a^3A_1 ($\sigma_{Co-R} \rightarrow \sigma_{Co-R}^*$), $a^{1,3}E$ and $b^{1,3}E$ MSBCT excited states and $c^{1,3}E$ and $b^{1,3}A_1$ MLCT excited states calculated at the equilibrium geometry and at bond distances of 50.0 Å for the Co-R and $Co-CO_{ax}$ bonds for $HCo(CO)_4$ (fig. 6.2a) and $CH_3Co(CO)_4$ (fig. 6.2b) are reported in table 6.3. The corresponding state correlation diagrams for $HCo(CO)_4$ and $CH_3Co(CO)_4$, depicted in figs. 6.4 and 6.3, respectively, present the connections between the low-lying electronic states at equilibrium and their corresponding states at dissociation that lead to the primary products $R^\bullet + {}^\bullet Co(CO)_4$ or $CO_{ax} + RCo(CO)_3$. Before discussing

State		Singlet			State		Triplet		
C_{3v} / C_s		equil	CO diss	R diss	C_{3v} / C_s		equil	CO diss	R diss
$HCo(CO)_4$									
a^1A_1	$^1A'$	1.1934	1.1330	1.0943			-	-	-
a^1E	$^1A'$	1.0120	1.0629	1.0553	a^3E	$^3A'$	1.0411	1.0888	1.0565
	$^1A''$	1.0089	1.0555	1.0539		$^3A''$	1.0464	1.0909	1.0561
b^1E	$^1A'$	0.9999	1.0390	1.0408	b^3E	$^3A'$	1.0280	1.0688	1.0438
	$^1A''$	0.9977	1.0392	1.0378		$^3A''$	1.0328	1.0698	1.0396
c^1E	$^1A'$	0.9847	-	0.9073	c^3E	$^3A'$	1.0065	-	0.9291
	$^1A''$	0.9887	-	0.9086		$^3A''$	1.0064	-	0.9298
b^1A_1	$^1A'$	0.9759	-	0.9007	b^3A_1	$^3A'$	1.0242	-	0.9402
					a^3A_1	$^3A'$	0.9724	-	1.0957
$CH_3Co(CO)_4$									
a^1A_1	$^1A'$	0.2090	0.1763	0.1493			-	-	-
a^1E	$^1A'$	0.0431	0.1074	0.1099	a^3E	$^3A'$	0.0724	0.1352	0.1096
	$^1A''$	0.0386	0.1019	0.1028		$^3A''$	0.0822	0.1314	0.1049
	-	-	-	-	a^3A_1	$^3A'$	0.0686	0.0844	0.1475
b^1E	$^1A'$	0.0258	0.1017	0.0965	b^3E	$^3A'$	0.0578	0.1278	0.0968
	$^1A''$	0.0254	0.0942	0.0896		$^3A''$	0.0600	0.1238	0.0905
c^1E	$^1A'$	0.0146	-	-	c^3E	$^3A'$	0.0261	-	-
	$^1A''$	0.0147	-	-		$^3A''$	0.0258	-	-
b^1A_1	$^1A'$	0.0047	-	-					

Table 6.3: CASSCF absolute energies in hartrees for the equilibrium and dissociation limits of $RCo(CO)_4$ (R=H, CH_3). The absolute energies are scaled by -1832. and -1872. E_h for $HCo(CO)_4$ and $CH_3Co(CO)_4$ respectively.

the state correlation diagrams based on CASSCF relative energies, the CASSCF transition energies to the low-lying singlet absorbing excited states should be compared to those obtained at the MS-CASPT2 level in the present work or in ref. [148] (table 6.4).

The relative order of the four low-lying singlet states (a^1E, b^1E, c^1E and b^1A_1) is not modified when going from the CASSCF to the MS-CASPT2 level and is qualitatively correct. The present MS-CASPT2 values differ from the previous theoretical study due to different CASSCF active spaces (16e13a or 16e14a used in section 6.1.2 vs. 10e14a used here). The present MS-CASPT2 values differ from the best values by more than 0.25 eV. The lowest a^1E and b^1E MSBCT absorbing states of $HCo(CO)_4$ calculated at 38450 cm^{-1}
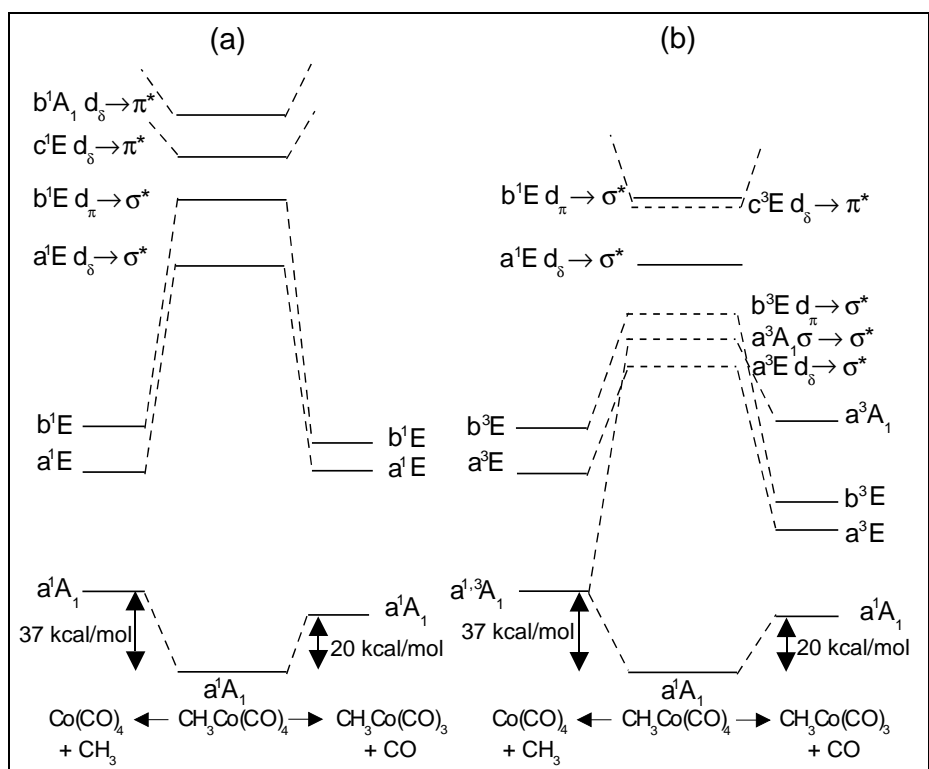
Figure 6.3: State correlation diagrams calculated at CASSCF level of theory for the singlet a) and triplet b) states of $CH_3Co(CO)_4$ for 5A′ and 4A″ roots.

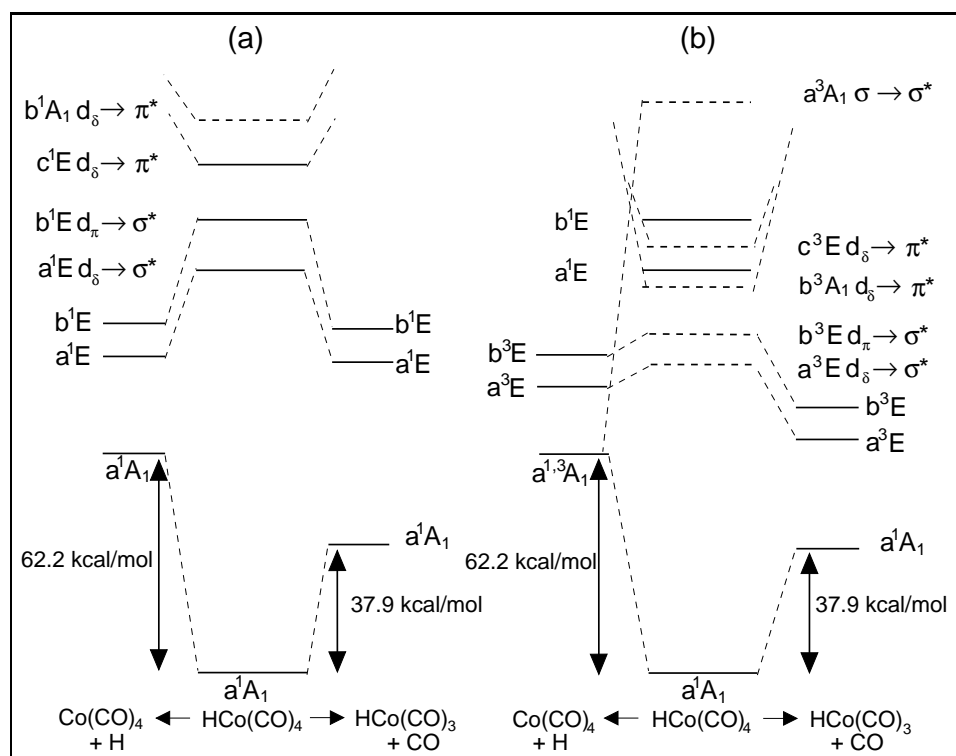**Figure 6.4:** State correlation diagrams calculated at CASSCF level of theory for the singlet a) and triplet b) states of $HCo(CO)_4$ for 9A′ and 8A″ roots.

State	Main Configuration	CASSCF(10,14)	MS-CASPT2	MS-CASPT2[a]
HCo(CO)$_4$				
a^{1}A$_1$ → a^{1}E	3d$_\delta$ → σ^*_{Co-R}	40150	38450	35740
a^{1}A$_1$ → b^{1}E	3d$_\pi$ → σ^*_{Co-R}	42710	41860	40280
a^{1}A$_1$ → c^{1}E	3d$_\delta$ → π^*_{CO}	45360	42880	41320
a^{1}A$_1$ → b^{1}A$_1$	3d$_\delta$ → π^*_{CO}	47730	44210	42040
CH$_3$Co(CO)$_4$				
a^{1}A$_1$ → a^{1}E	3d$_\delta$ → σ^*_{Co-R}	36910 (37230)[b]	32410	33980
a^{1}A$_1$ → b^{1}E	3d$_\pi$ → σ^*_{Co-R}	40250 (39000)[b]	35960	38390
a^{1}A$_1$ → c^{1}E	3d$_\delta$ → π^*_{CO}	42660 (43670)[b]	39660	40720
a^{1}A$_1$ → b^{1}A$_1$	3d$_\delta$ → π^*_{CO}	44840 (54870)[b]	41560	42340

[a] Data from section 6.1.2.

[b] Values in parenthesis correspond to CASSCF(10,12) and A$'$ symmetry.

Table 6.4: CASSCF and MS-CASPT2 transition energies, given in h·c·cm^{-1}, for the low-lying singlet absorbing states of HCo(CO)$_4$ and CH$_3$Co(CO)$_4$.

and 41860 cm^{-1} at the MS-CASPT2 level (35740 cm^{-1} and 40280 cm^{-1} in section 6.1.2) are dissociative with respect to the homolysis of the cobalt-hydrogen bond as well as to the dissociation of the axial carbonyl, see fig. 6.4. The upper MLCT states (c^{1}E, b^{1}A$_1$) are bound and should not participate in the UV photoreactivity of HCo(CO)$_4$. The photofragmentation of the molecule in gas phase, in a direct and ultrafast mechanism that forms the primary products H + Co(CO)$_4$ and CO + HCo(CO)$_3$ within a few hundred femtoseconds after UV irradiation, is highly probable. When the triplet states are taken into account, see fig. 6.4b, the photodissociation may occur via intersystem crossing from the a,b^{1}E absorbing states to the low-lying a^{3}E, b^{3}E and ^{3}A$_1$ states, all of which are dissociative. In particular, the a^{3}A$_1$ (σ_{Co-H} → σ^*_{Co-H}) state will lead to the H$^\bullet$ + $^\bullet$Co(CO)$_4$ (^{1,3}A$_1$) diradical primary products according to the mechanism proposed in ref [22, 149]. This mechanism, in contrast to a direct ultrafast deactivation via the singlet absorbing states, will occur on a picosecond time-scale. The lowest a^{1}E and b^{1}E MSBCT absorbing states of CH$_3$Co(CO)$_4$ calculated at 32410 cm^{-1} and 35960 cm^{-1} at the MS-CASPT2 level (33980 cm^{-1} and 38390 cm^{-1} in section 6.1.2) are clearly dissociative for both channels, namely the homolysis of the Co-CH$_3$ bond and the loss of the axial carbonyl, as can be seen in fig. 6.3. The upper c^{1}E and b^{1}A$_1$ MLCT states are bound and no correlation was found with the low-lying states at dissociation. The mechanism of ultrafast gas phase photofragmentation based on the low-lying singlet states is similar to the one proposed

for HCo(CO)$_4$ leading to $^\bullet$CH$_3$ + $^\bullet$Co(CO)$_4$ and CO + CH$_3$Co(CO)$_3$ fragments within a few hundred femtoseconds. Again the a^{3}A$_1$ ($\sigma_{Co-CH_3} \rightarrow \sigma^*_{Co-CH_3}$) will play a key role in the formation of the diradical primary products within picoseconds after intersystem crossing.

Two-dimensional Potential Energy Surfaces and Photoactivity   In order to investigate in more detail the mechanism of ultrafast photodissociation of both molecules the 2-D adiabatic potential energy surfaces have been built as a function of the metal-R (q$_1$) and metal-CO$_{ax}$ (q$_2$) bond distances for the a^{1}A$_1$ electronic ground state and the four low-lying MSBCT (a^{1}E and b^{1}E) and MLCT states (c^{1}E and b^{1}A$_1$). The 1-D cuts along q$_1$ and q$_2$ are shown in fig. 6.5 (for R=H cf. ref. [21]). As predicted from the state-correlation diagrams shown in figs. 6.3 and 6.4, the two lowest MSBCT (a^{1}E and b^{1}E) states are strongly repulsive along both dissociation channels. At the Franck-Condon (FC) region the gradients are steeper and lower in energy along the Co-R bond coordinate, and therefore dissociation of H or CH$_3$ should be faster than Co-CO. This is confirmed by propagating the initial vibrational ground state wave function on any of the MSBCT surfaces, and watching the autocorrelation function, which is an indicator of the rate at which dissociation occurs.
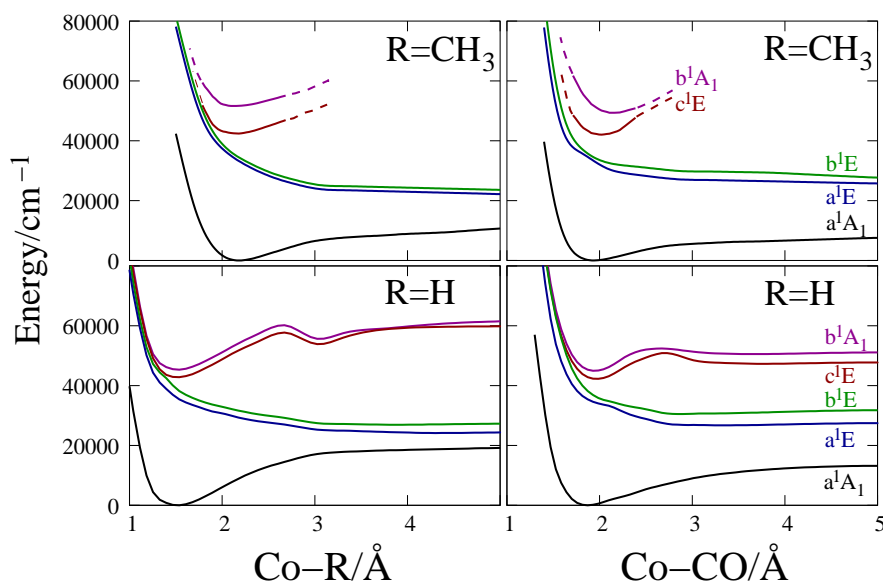

Figure 6.5: One-dimensional potential energy cuts along the equilibrium q$_1$(Co-R) and q$_2$(Co-CO) coordinates for the five lowest-lying electronic states of HCo(CO)$_4$ (cf. ref. [21]) and CH$_3$Co(CO)$_4$.

Figure 6.6: The decay time of the autocorrelation function is measured on the a^1E state for a) $HCo(CO)_4$ and b) $CH_3Co(CO)_4$ with corresponding values of 3.4 fs and 5.3 fs respectively at 1/e. The potential is completely dissociative and therefore there are no recurrences of the wavepacket.
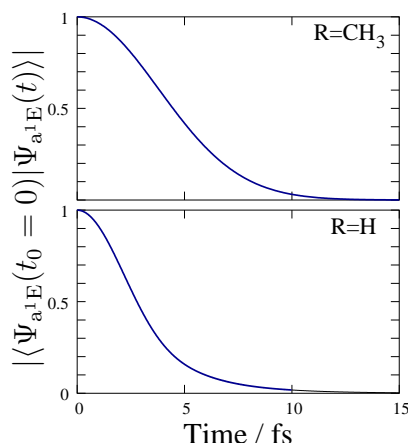
Exemplary, the autocorrelation functions $S_j(t)$ on the repulsive a^1E state are shown in fig. 6.6. For $HCo(CO)_4$, dissociation occurs along the H channel and $S_{a^1E}(t)$ reaches the reciprocal of e after 3.4 fs. In $CH_3Co(CO)_4$, the same value is reached after 5.3 fs and both the CO and CH_3 are fragmented. According to the bounded shape of the upper MLCT states (c^1E and b^1A_1), the system will be trapped in their corresponding potential wells when these states are populated and energy will be redistributed among other vibrational modes. The minima in the MLCT states, c^1E and b^1A_1, are located at q_1=1.552, q_2=1.999 Å and q_1=1.552, q_2=1.905 Å for $HCo(CO)_4$ and q_1=2.195, q_2=2.026 Å and q_1=2.195, q_2=2.169 Å, for $CH_3Co(CO)_4$, respectively. These MLCT states are also characterized by several avoided crossings before 3 Å, more clearly depicted in the case of $HCo(CO)_4$ for which the c^1E, b^1A_1 states have been computed until dissociation. The avoided crossings appear far enough away from the minima so that upon a vertical excitation, the wavepacket does not have enough kinetic energy to overcome the barrier, and consequently, the system will not explore this region of the adiabatic PESs. The non-adiabatic couplings will not be taken into account within the limit of short time-scale simulations, although diabatic couplings may be important.

6.1.4 Eigenfunctions

Computational Details

The eigenvalues and eigenfunctions of the two complexes have been calculated using the FGH method [69, 70] using the WavePacket program package [83] as discussed in section 2.3.1. The Hamiltonian employed in the calculation is a sum of the kinetic energy $\hat{T}_{nu}$ and

the potential energy $\hat{\mathbf{V}}_g$ operators. The potential energy is represented by the adiabatic potential energy surfaces, shown in fig. 6.5 and the kinetic energy operator for a reduced 2-D model [21] is given by

$$\hat{\mathbf{T}}_{\text{nu}} = -\frac{\hbar^2}{2m_1}\frac{\partial^2}{\partial q_1^2} - \frac{\hbar^2}{2m_2}\frac{\partial^2}{\partial q_2^2} + \frac{\hbar^2}{m_{\text{Co(CO)}_3}}\frac{\partial}{\partial q_1}\frac{\partial}{\partial q_2} \tag{6.1}$$

with the following reduced masses

$$m_1 = \frac{m_{\text{R}} \cdot m_{\text{Co(CO)}_3}}{m_{\text{R}} + m_{\text{Co(CO)}_3}} \qquad \text{and} \qquad m_2 = \frac{m_{\text{CO}} \cdot m_{\text{Co(CO)}_3}}{m_{\text{CO}} + m_{\text{Co(CO)}_3}} \tag{6.2}$$

where R=H, CH$_3$. Accordingly, the reduced mass m_1 is 0.99 amu and 13.58 amu for HCo(CO)$_4$ and CH$_3$Co(CO)$_4$ respectively, and m_2 is equal to 23.41 amu for both complexes. Each calculation was carried out on a regularly spaced grid containing 64 points along each coordinate (64×64 = 4096 points) for both systems. These points were divided up between 1.0 Å and 1.47 Å along the q$_1$ coordinate and 1.5 Å and 2.49 Å along the q$_2$ coordinate for HCo(CO)$_4$ and 1.8 Å and 3.2 Å along the q$_1$ coordinate and 1.72 Å and 3.02 Å along the q$_2$ coordinate for the CH$_3$Co(CO)$_4$, as given in table 6.5.

	Eigenfunction	Propagation
HCo(CO)$_4$		
q$_1$=d(Co-R)	1.00 to 2.47 Å(64 points)	1.00 to 24.52 Å(1024 points)
q$_2$=d(Co-CO)	1.50 to 2.49 Å(64 points)	1.50 to 3.48 Å(128 points)
CH$_3$Co(CO)$_4$		
q$_1$=d(Co-R)	1.80 to 3.20 Å(64 points)	1.80 to 7.40 Å(256 points)
q$_2$=d(Co-CO)	1.72 to 3.02 Å(64 points)	1.72 to 6.92 Å(256 points)

Table 6.5: Regular spatial grids employed for the calculation of the initial eigenfunction and for the propagation of the wave function in the 2-D PES of HCo(CO)$_4$ and CH$_3$Co(CO)$_4$. The number of grid points along one dimension in each case is indicated in parenthesis.

Results

Eigenvalues and Eigenfunctions   The twelve lowest-lying eigenfunctions for HCo(CO)$_4$ and CH$_3$Co(CO)$_4$ are plotted on the contours of the ground state a^{1}A$_1$ PES in figs. 6.7 and 6.8 and their corresponding eigenvalues are tabulated in table 6.6. The notation for the vibrational eigenfunctions is simplified in the following by the replacement of Ψ_j^v with the

vibrational quantum number $v_{q_1 q_2}$, defined in two-dimensions with coordinates q_1 and q_2. The ground state eigenfunction is therefore denoted as v_{00}, the fundamental stretching mode of the Co-R bond is denoted as v_{10}, and v_{01} represents the stretching mode of Co-CO$_{ax}$.

The effects of the PES and kinetic energy coupling of the two coordinates, see eq. 6.1, can be visualized in fig. 6.8, by the curvature of the nodal planes. The eigenfunctions for HCo(CO)$_4$ indicate a decoupling of the modes; the nodal planes are perpendicular or parallel to either the q_1 or q_2 axes. This characteristic is due to the large mass difference between the two ligands. The vibrational frequency for the fundamental mode v_{01} corresponding to the decoupled axial carbonyl stretching is $\nu_{01} = 374$ cm^{-1}, see table 6.6 and is comparable to the corresponding harmonic DFT frequency value using the B3LYP function of 409 cm^{-1} computed on the DFT optimized structure. The eigenvalue for the fundamental Co-H stretching mode (v_{10}) has an energy of E$_{10}$ = 2750 cm^{-1} with a vibrational frequency of ν_{10} = 1710 cm^{-1} also very close to the harmonic DFT multidimensional value of 1713 cm^{-1}. The Co-H vibrational frequency has been measured experimentally in the gas phase at 1934 cm^{-1} [150], which implies a difference of ca. 200 cm^{-1} due to anharmonicity. The similarity of the two calculated values for the ν_{10} vibrational frequency indicates that this mode calculated from the ground state PES is represented well by the DFT harmonic calculations.

The eigenfunctions for CH$_3$Co(CO)$_4$ in the reduced 2-D representation indicate a strong coupling between the two vibrational modes. This appears as a deviation of the nodal planes away from the uncoupled case, e.g. the hydrido complex, compare fig. 6.8 with 6.7. The calculated eigenvalue and vibrational frequency for the fundamental mode v_{01} for the methyl-cobalt bond is E$_{01}$=796 cm^{-1} and ν_{01}=309 cm^{-1}, respectively. The DFT frequency calculation retrieved a value of 424 cm^{-1} for the harmonic vibrational frequency. The deviation is 115 cm^{-1} and is due to the minimal description of the molecule and because this vibrational mode is coupled to the C=O stretching mode, which is not accounted for in this work. The vibrational frequency for the fundamental Co-CO stretch is calculated as ν_{10} = 484 cm^{-1} which is similar to the harmonic DFT calculation at 473 cm^{-1}, indicating its similarity to the harmonic value. At low vibrational energies this concurrence with the harmonic values are expected. The fundamental frequencies, ν_{01} and ν_{10} correspond to the symmetric and anti-symmetric stretching, due to their coupled motion. The experimental vibrational modes for CH$_3$Co(CO)$_4$ are not available.
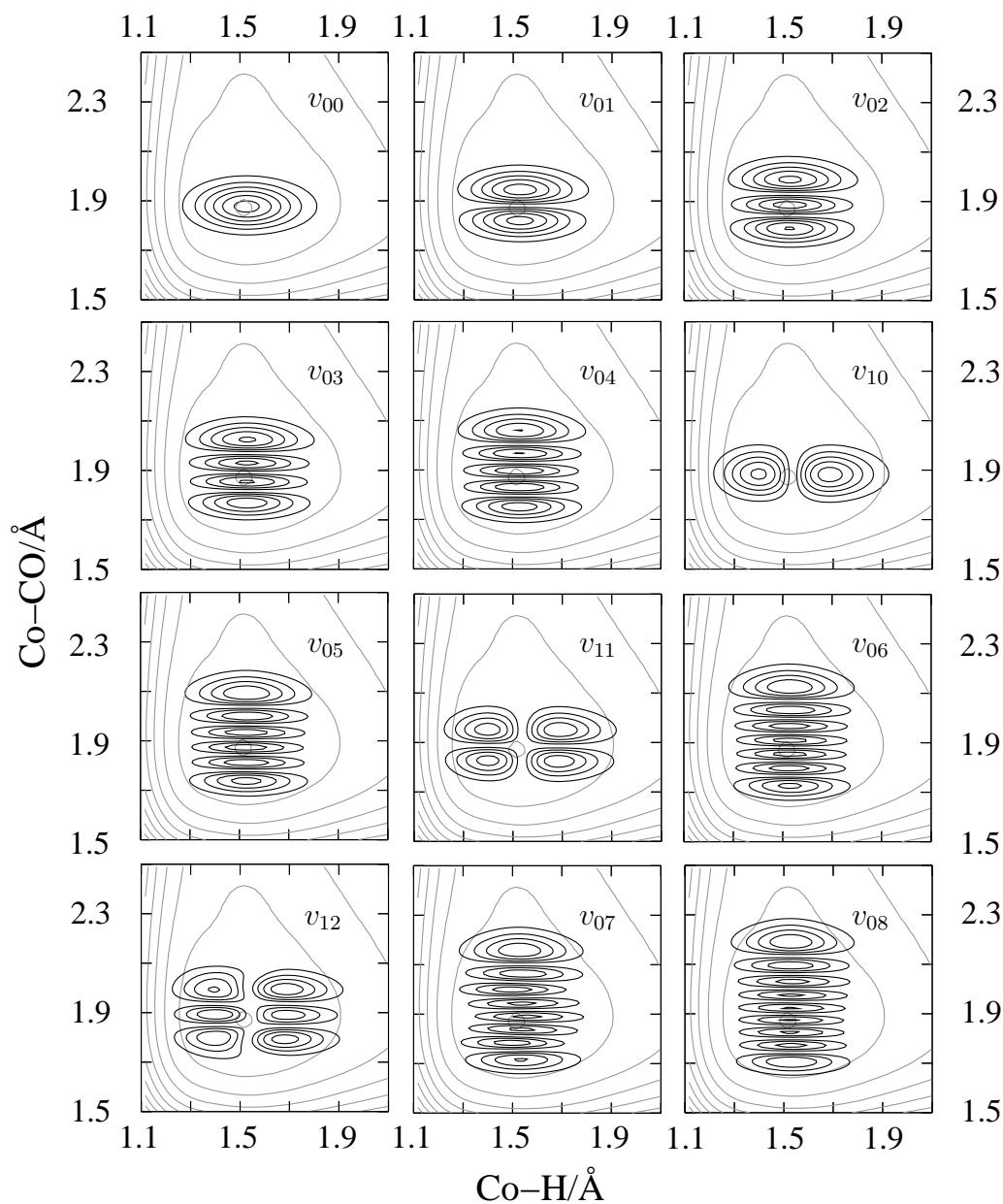
Figure 6.7: Two-dimensional contour plots of the first 12 eigenfunctions for the ground electronic state, a^1A_1 of $HCo(CO)_4$. Each eigenfunction is labeled according to its quantum number $v_{q_1q_2}$, where q_1 and q_2 correspond to the Co-H and Co-CO bond respectively.
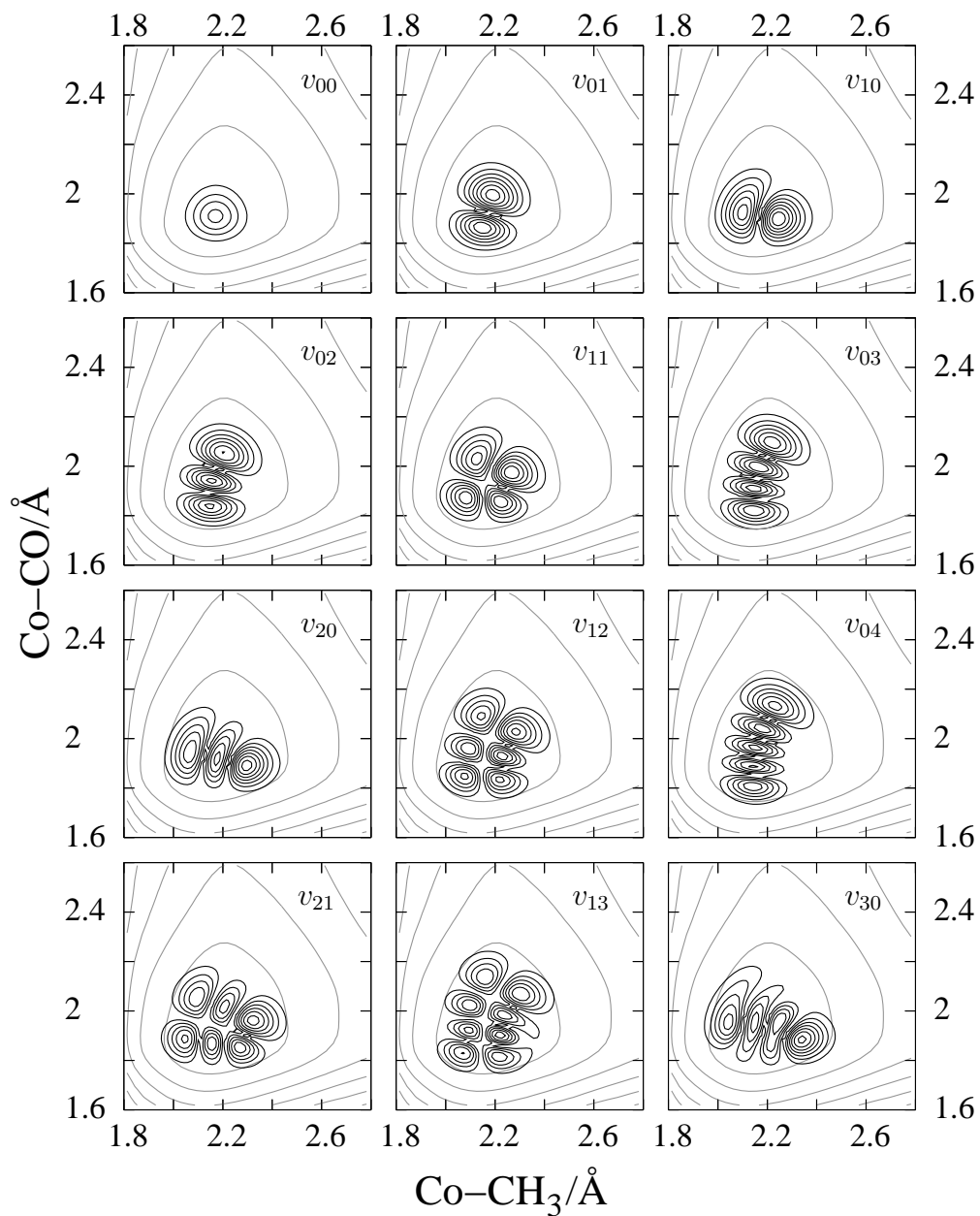
Figure 6.8: Two-dimensional contour plots of the first 12 eigenfunctions for the ground electronic state, a^1A_1 of $CH_3Co(CO)_4$. Each eigenfunction is labeled according to its quantum number $v_{q_1q_2}$, where q_1 and q_2 correspond to the Co-H and Co-CO bond respectively.

| $v_{q_1 q_2}$ [a] | HCo(CO)$_4$ | | | $v_{q_1 q_2}$ [a] | CH$_3$Co(CO)$_4$ | | |
	Energy	ν [b]	ν [c]		Energy	ν [b]	ν [c]
v_{00}	1040	-		v_{00}	487	-	
v_{01}	1414	374	409	v_{01}	796	309	424
v_{02}	1786	372		v_{10}	971	484	473
v_{03}	2150	364		v_{02}	1087	291	
v_{04}	2506	356		v_{11}	1272	-	
v_{10}	2750	1710	1713	v_{03}	1376	289	
v_{05}	2849	343		v_{20}	1426	455	
v_{11}	3120	-		v_{12}	1559	-	
v_{06}	3180	331		v_{04}	1664	288	
v_{12}	3491	-		v_{21}	1717	-	
v_{07}	3500	320		v_{13}	1842	-	
v_{08}	3808	308		v_{30}	1855	429	

[a] Vibrational mode

[b] Vibrational frequency

[c] Harmonic DFT values calculated using the B3LYP functional
    and the 6-31G(d) basis set.

Table 6.6: Tabulated eigenenergies, E, and vibrational frequencies, ν, given in cm^{-1} for the twelve low-lying eigenfunctions for HCo(CO)$_4$ and CH$_3$Co(CO)$_4$.

The harmonicity of the ground state adiabatic PES is investigated by comparing the vibrational frequencies for sequential vibrational modes, i.e. addition of one quanta into a single mode. For the HCo(CO)$_4$ complex, the carbonyl-cobalt stretching modes are rather similar in frequency, see table 6.6. The first two corresponding vibrational frequencies, i.e. ν_{01} and ν_{02}, differ no more than 2 cm^{-1}, again indicating the harmonic characteristic around the equilibrium geometry. The higher-lying vibrational frequencies differ significantly from the corresponding fundamental vibrational frequency, e.g. $\nu_{08} = 308$ cm^{-1} vs. $\nu_{01} = 374$ cm^{-1} indicating that the overall structure of the ground state PES is anharmonic. The anharmonic structure of the methyl complex ground state PES is more pronounced, see fig. 6.5 and table 6.6, and can be deduced from the vibrational frequencies as was done for HCo(CO)$_4$.

6.2   Quantum Dynamics

The theoretical absorption spectra of both complexes will be presented in this section. The discussion will proceed by analyzing the wavepacket dynamics on the bound electronic states that contribute most strongly to the absorption spectra. This section will close by analyzing the wavepacket dynamics on the remaining states upon a vertical transition. The field-free evolution will be termed the natural dynamics.

6.2.1   Theoretical Absorption Spectra

Computational Details

The UV absorption spectra were calculated using a time-dependent approach as proposed by Heller [75]. Equation 3.29 describes the calculation of the absorption spectrum as a Fourier transform of the autocorrelation function, $S_{tot}(t)$, which is obtained from the temporally propagated wavepacket by solving the time-dependent Schrödinger equation 3.1. The applied Hamiltonian, $\hat{H}$, is composed of the kinetic, $\hat{T}_{nu}$, and potential, $\hat{V}_{el}$, energy operators as discussed in section 6.1.4. The ground vibrational eigenfunction is calculated using the Fourier Grid Hamiltonian method [69] with a spatial discretization of $64\times64 = 4096$ grid points, see section 6.1.4. The time-dependent propagation of the wave function is carried out on larger grids of $256\times256 = 65536$ for the methyl complex and $128\times1024 = 131072$ grid points for the hydrido complex, as indicated in table 6.5, using the split-operator method [79] as implemented in the WavePacket set of programs, [83], with a time step of 0.01 fs over 1 ps. In order to avoid unphysical reflections of the wave functions, an absorbing boundary potential [81] has been established at 6.40 and 6.00 Å for the methyl complex and 23.0 and 3.3 Å for the hydrido complex along the q_1 and q_2 coordinates, respectively, see eq. 3.46 for its form. The initial wavepacket on the upper electronic state, j, is a dipole weighted ground state wave function, i.e. a wave function that has been multiplied by a normalized transition dipole moment, see eqs. 3.30 and 3.31. The TDM have been calculated at the CASSCF level in accordance with the PESs and have been normalized according to eq. 3.31. The transition dipole functions are set to a constant value taken at the Franck-Condon point and are given in atomic units (ea_0) $\boldsymbol{\mu}_{21} = 0.117, 0.186$; $\boldsymbol{\mu}_{31} = 0.108, 0.110$; $\boldsymbol{\mu}_{41} = 0.457, 0.479$; $\boldsymbol{\mu}_{51} = 0.318, 0.225$;

respectively for $HCo(CO)_4$ and $CH_3Co(CO)_4$, where the indexing follows the order of the electronic states from the lowest to the highest energy, e.g. $\boldsymbol{\mu}_{21}$ corresponds to a TDM between the ground electronic state a^1A_1 (1) and a^1E the second (2) electronic state.

Results

Time-dependent Absorption Spectra   The normalized absorption spectra for $RCo(CO)_4$ are calculated via time-dependent wavepacket propagations on adiabatic 2-D surfaces and are shown in fig. 6.9. For both complexes, the spectra are characterized by two main bands, which correspond to the bound c^1E and b^1A_1 MLCT states, with respective vibrational progressions for the metal-ligand stretching modes. As expected, the band positions agree well with the CASSCF values listed in table 6.4.

For $HCo(CO)_4$ (bottom spectrum in fig. 6.9, cf. ref. [21]), the first band corresponds to the c^1E state and stretches from 42280 to 44700 cm^{-1}; the second band corresponds to the b^1A_1 state and extends from 45000 to 47100 cm^{-1}. The absorption spectrum of $HCo(CO)_4$ is not directly comparable to the experimental absorption spectrum recorded in an argon matrix [151] which is characterized by an intense band between 36000 cm^{-1} and 43480 cm^{-1}. The maximum peaks of the calculated spectrum are observed at 42660 cm^{-1} and at 45000 cm^{-1} for the c^1E and b^1A_1 bands, respectively. That the peak maxima appear at the low energy part of the spectrum can be explained by the fact that the minimum of the c^1E and b^1A_1 states is nearly coincident with that of the electronic ground state (see fig. 6.5) and therefore, the initial wave function overlaps greatest with the lowest vibrational levels. Specifically, the maximum overlap is achieved with the second and first vibrational levels of the c^1E and b^1A_1 states, respectively. Within the precision that the simulation allows (number of sampling points in the region of interest), the separation between the peaks is rather regular (ca. 400 cm^{-1}) in both bands, and corresponds to the Co-CO stretching vibration. This is in agreement with the spacing seen with the overtones v_{0q_2} in table 6.6.

The theoretical spectrum of $CH_3Co(CO)_4$ (top spectrum in fig. 6.9) also presents two bands associated to the bound c^1E and b^1A_1 states, though the shape of the bands differs from those of $HCo(CO)_4$. The lowest energy band, extending from 42580 to 43800 cm^{-1} is more intense than the broader higher energy band, which appears between 50000 and 55000 cm^{-1}. The relative intensities are due to the different transition dipole moments
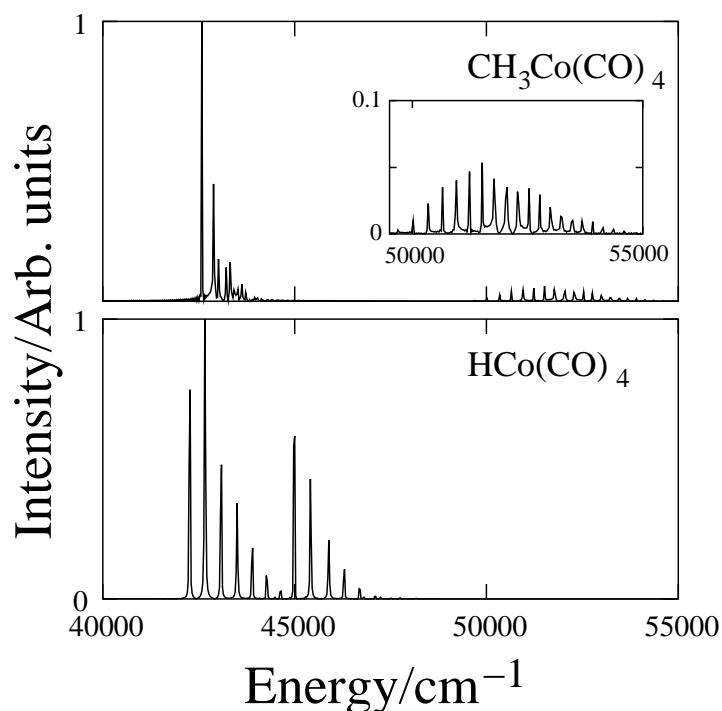
Figure 6.9: Normalized theoretical absorption spectra for the RCo(CO)$_4$ complexes (for R=H, cf. ref. [21]).

as well as the amount of overlap with the corresponding vibrational levels of the c^{1}E and b^{1}A$_1$ states (cf. eqs. 3.30 and 3.31). The band positions are shifted with respect to the MS-CASPT2 energies (cf. table 6.1); however, the qualitative structure of the peaks should acquiesce independent of the employed method. Interestingly, the first band (peaking at 42600 cm^{-1}) does not show regular spacing as in HCo(CO)$_4$. This is due to the overlap of the initial wave function with the one propagated in time: the autocorrelation function. The evolving wave function constantly overlaps with the initial wave function along both degrees of freedom which affects the shape of the autocorrelation function and creates a complicated absorption spectrum. The initial wave function superimposed on the c^{1}E potential along with the trajectory of the center of the wavepacket evolving over 1 ps, is shown on the left in fig. 6.10. As can be seen, the motion of the wavepacket is focused within a small region, consistently overlapping with the original wave function as it moves over the PES in a pathway shaped like a pretzel. It moves in a more complex fashion, compared to a simple one-directional motion, which is responsible for the irregular spacing in the first band. In contrast, the motion of the wavepacket in the b^{1}A$_1$ state (cf. right of fig. 6.10) is nearly only along the Co-CO stretching coordinate in which the wavepacket moves farther away from its original position; upon its return, its overlap with

the initial wave function is significantly smaller than in its c^1E counterpart which accounts for the low intensities of these peaks. This autocorrelation function consequently tracks the overlap occurring along one vibrational coordinate, i.e. Co-CO, and therefore the second band (peaking at 52050 cm^{-1}) shows a regular spacing of about ca. 300 cm^{-1} that corresponds to the Co-CO vibration in the b^1A_1 state, see inset of fig. 6.9 and table 6.6.
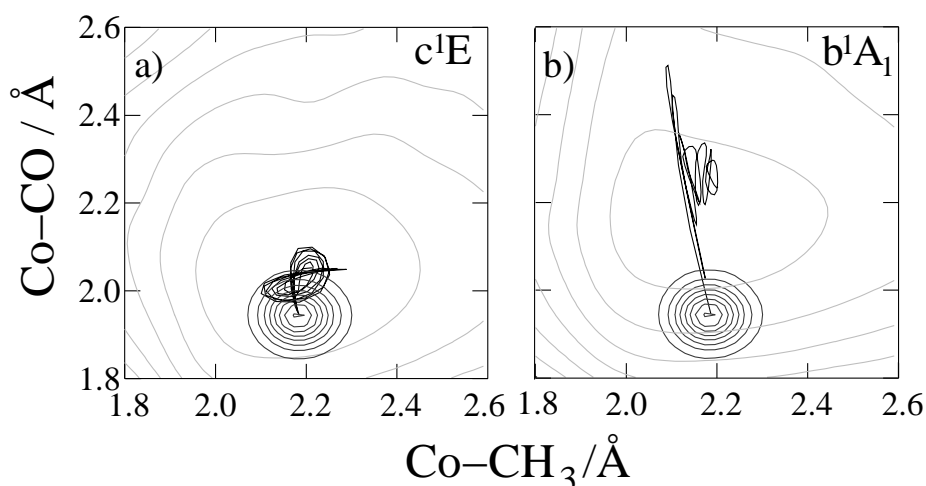

Figure 6.10: Contours of the initial wave function superimposed on a) the c^1E and b) the b^1A_1 2-D potential energy surfaces along the q_1=Co-CH$_3$ and q_2=Co-CO coordinates of CH$_3$Co(CO)$_4$. The plotted trajectory is the trace of the center of mass of the corresponding time-dependent wavepacket evolving over 1 ps.

6.2.2 Wavepacket Dynamics

Of particular interest is the natural dynamics of the wavepacket on each of the PESs. Much information on the dynamics has already been ascertained through analysis of the 1-D cuts at the equilibrium position of the ground state. According to the Franck-Condon principle, a vertical transition occurs from the ground state to any of the dipole allowed excited states at the same molecular geometry. At this position, the wavepacket is influenced solely by the slope of the surface in both position and momentum space, since the transferred kinetic energy is zero; the initial wave function is the ground vibrational state, $\Psi_0 = v_{00}$, located in the ground electronic state and has zero kinetic energy. The first two unbound states a^1E and b^1E are clearly dissociative for both complexes.

The field-free evolution of the wavepackets on the unbound electronic states is investigated for $HCo(CO)_4$. The initial wavepackets are prepared by multiplying the ground state wave function Ψ_0 with the transition dipole moment at the Franck-Condon point and are excited via a δ pulse. The dynamics that ensue on the a^1E and b^1E states describe a pure dissociation of the complex into the radical products, $H^\bullet + {}^\bullet Co(CO)_4$. This behavior is controlled completely by its Hamiltonian in a dual relationship between the kinetic and potential energy. Due to the extreme lightness of the hydrogen ligand compared to the carbonyl ligand, the momentum space is very narrow and steep in the H-Co coordinate and rather spread out for the Co-CO coordinate. The narrowness of the momentum space in the H-Co coordinate along with the gradient of the PES at the Franck-Condon window prefers a 100% dissociation of the hydride.

The evolution of the wavepacket on the bound states c^1E and b^1A_1 of $CH_3Co(CO)_4$ was analyzed in section 6.2.1 for the discussion of the absorption spectra (see fig. 6.10), by tracing the temporal motion of the center of the wavepacket. The wavepacket's evolution on the unbound states (a^1E and b^1E) is of particular interest for the dissociation of either of the two ligands, CH_3 or CO. Upon a vertical transition, the wavepacket on either of these two states prefers to traverse diagonally across the unbound state: breaking both bonds. The structure of the unbound states is not characterized by two distinct dissociation channels. In fact, the surface spreads out into an open plane, slightly tilted in the favor of elongation of the $Co-CH_3$ bond. Consequently, the motion of the wavepacket is strongly influenced by its momentum, and due to the similarities in mass of the two ligands, dissociation occurs for both ligands.

The simultaneous breakage of two bonds based on the rather structureless electronic surface poses a new playground for control. Rather than controlling the percentage of the wavepacket that exits via one dissociation channel versus the other, as done in all works available up to date in the literature, here the control will focus on preventing the concerted breakage of two bonds by steering the wavepacket specifically in either of the two dissociation pathways breaking either the $Co-CH_3$ or the Co-CO bond.

6.3   Quantum Control

Coherent control of the concerted two bond breakage of the CH_3 and the CO ligands in the $CH_3Co(CO)_4$ complex is investigated. As discussed in section 6.2.2, the natural temporal evolution of the wavepacket under light radiation on the a^1E and b^1E unbound surfaces corresponds to a simultaneous bond breakage of both ligands, in contrast to what has been observed in most of the organometallic complexes studied until now, i.e. breaking of the weaker bond. The potential energy surfaces lack distinct dissociation channels along both coordinates, and therefore, the wavepacket is not influenced by the barriers and may move diagonally across the potential surface. The wavepacket's diagonal evolution on the a^1E electronic surface upon a delta-laser pulse excitation is plotted in fig. 6.11 at intervals of 25 fs, to display the simultaneous breakage of both ligand bonds. The temporal evolution on the b^1E is similar.
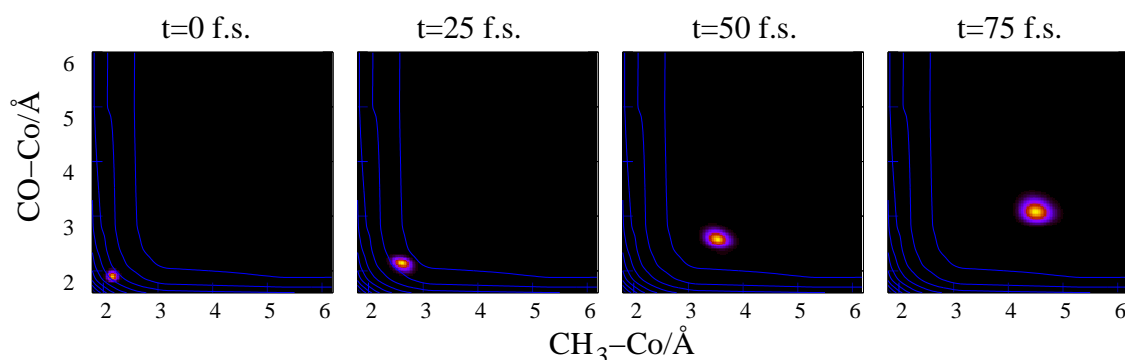

Figure 6.11: Snapshots of the wavepacket on the unbound a^1E electronic state upon a delta-laser pulse excitation at t=0, 25, 50 and 75 fs.

Due to the contour of the unbound surface the wavepacket moves together in the same direction, i.e. does not split, and spreads out as it moves away from the equilibrium geometry. Because the wavepacket moves as a whole at an angle away from the Franck-Condon point the question of control we pose here is not, "How can one increase the percent of dissociation of one ligand with respect to the other?" but rather, "Is it possible to control the system to produce a single bond breakage instead of a simultaneous two bond breakage?". In order to quantify the extent to which the system is controlled in this novel system, it is advantageous to define an appropriate method.

6.3.1   Control Measures

Two methods to quantify the amount of control for competing ligand dissociation are discussed here: the branching ratio and angle of dissociation. The branching ratio is a standard measure of control used for molecular systems whose unbound surface is characterized by distinct dissociation channels. The angle of dissociation is introduced in this work as a customized measure of control which is applied to dissociation on unbound states that lack the distinct dissociation channels.

Branching ratio   The branching ratio is a standard measure of control for molecular systems whose unbound states are characterized by two dissociation channels. Consider a general, linear, A-B-C triatomic molecule whose unbound electronic surface is characterized by two exit channels, as depicted in fig. 6.12a. Upon excitation, the molecule has the possibility to dissociate in either of two pathways, either in channel A or in channel B. Dissociation on these types of surfaces results typically in a division of the wavepacket into the two channels. The applied quantifier of control is the branching ratio, which is a ratio of the amount of population in channel A with respect to channel B, at a final time, t_f, and can be defined as

$$\text{Branching Ratio} = \frac{\text{Pop}_{j,A}(t_f)}{\text{Pop}_{j,B}(t_f)}. \tag{6.3}$$

The population that is located in either channel on the electronic state j at the end of the propagation, t_f, is defined as

$$\text{Pop}_{j,\text{C}}(t_f) = \langle \Psi_j(t_f) | \hat{P}_\text{C} | \Psi_j(t_f) \rangle \tag{6.4}$$

where $\hat{P}_\text{C}$ is a projection operator, and C denotes either channel A or channel B. The step function, Θ, is used to define the boundary conditions for each channel and is given below specifically for the A channel

$$\hat{P}_A = \Theta \begin{cases} 1 & \text{if} \quad x > x_d \quad \text{and} \quad y < y_d \\ 0 & \text{else} \end{cases} \tag{6.5}$$

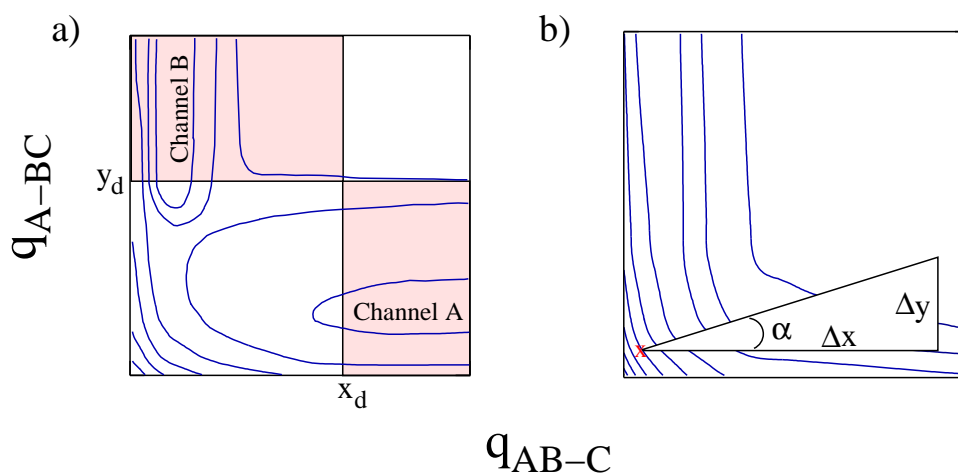A similar relation is used for channel B in which the binary relations in the step function are reversed.

Figure 6.12: Depiction of two control quantifiers for an ABC molecule: a) the branching ratio, and b) the angle of dissociation, α. The branching ratio is the ratio of the population in one channel versus the other channel. The channels are defined at a specific bond elongation denoted as x_d and y_d along the two stretching coordinates q_{AB-C} and q_{A-BC}, respectively. The angle of dissociation is defined as the arctangent of the displacement of the center of mass of the wavepacket along q_{A-BC}, symbolized as Δy, divided by the displacement along the q_{AB-C} coordinate, symbolized as Δx.

Angle of dissociation   For the special case in which the unbound state lacks specific dissociation channels, as seen in fig. 6.12b, a new approach to quantify the control is introduced: the angle of dissociation. Consider again the linear triatomic molecule, ABC. In order to apply this approach it is necessary to trace the center of the wavepacket over time from its initial position on the electronic state j. This is done by calculating the expectation value of its position,

$$\langle \mathbf{r}_j \rangle = \langle \Psi_j(t) | \hat{\mathbf{r}} | \Psi_j(t) \rangle \tag{6.6}$$

where $\hat{\mathbf{r}}$ represents the coordinate operators $\hat{\mathbf{x}}$ and $\hat{\mathbf{y}}$. The angle of dissociation can now be given in the following form,

$$\alpha = \arctan\left(\frac{\Delta y}{\Delta x}\right) \tag{6.7}$$

where Δy is defined as the displacement of the wavepacket along the q_{A-BC} coordinate and Δx is the displacement along the q_{AB-C} coordinate, as depicted in fig. 6.12. The x-mark on the contour surface indicates the initial position at the Franck-Condon point. The angle $\alpha = 90°$ corresponds to the A-BC single bond breakage, and the angle $\alpha = 0°$ corresponds to the breakage of the AB-C bond. The angles in-between correspond to a concerted breakage of both bonds, with different velocities for $\alpha \neq 45°$.

6.3.2   Pump-Dump Control Mechanism

Computational Details

The pump-dump control mechanism that is investigated in this work, see fig. 4.3, employs the following three electronic states: the ground electronic state a^1A_1, and the two excited electronic states, a^1E and b^1A_1, see fig. 6.5. The selection of the b^1A_1 state is based on field-free wavepacket dynamics, see section 6.2.2, which indicate an elongation of the Co-CO bond while the CH_3-Co bond is left rather unaffected, as can be seen on the right in fig. 6.10b. The unbound excited state used in the simulation was chosen as the a^1E state, though the b^1E could also have been used since the two surfaces are rather similar. Based on the topography of these states, the following control strategy can be devised. Pumping population from the ground a^1A_1 to the bound b^1A_1 electronic state will cause an elongation of the Co-CO bond. A dump pulse will transfer the population to the unbound a^1E electronic state. As was seen in the natural dynamics, the wavepacket evolves diagonally across the unbound a^1E state, depicting a simultaneous dissociation of both ligands. Using a well-timed dump pulse it should be possible to steer the evolution of the wavepacket on the unbound state in such a way that only one of the two ligands dissociate, i.e. either CO or CH_3.

The pump-dump quantum dynamic simulations for $CH_3Co(CO)_4$ were carried out using a constant transition dipole function on a regular spatial grid of $256 \times 256 = 65536$ points, using WavePacket program package [83]. The points were distributed between 1.80 and 7.40 Å for the q_1 coordinate and 1.72 and 6.92 Å for the q_2 coordinate. For the notation of the TDM, the ground state a^1A_1 will be denoted as the first (1) electronic state, the a^1E will be denoted as the second (2) electronic state, and the b^1A_1 will be denoted as the fifth (5) electronic state, maintaining the same ordering of states starting from the lowest energy. The TDM, in atomic units (ea_0), corresponding to the three electronic states of interest are $\boldsymbol{\mu}_{21} = -0.1138, -0.0082$; $\boldsymbol{\mu}_{51} = -0.0703, -0.2011$; $\boldsymbol{\mu}_{25} = -0.0548, -0.0013$ for the x and z components respectively. A z-polarized pump pulse has been selected based on the relatively large transition dipole moment of $\boldsymbol{\mu}_{51} = -0.2011$, and the dump pulse, used to transfer population from the b^1A_1 to the a^1E state has a more significant TDM in the x component of $\boldsymbol{\mu}_{25} = -0.0548$, and therefore is x-polarized. The electric field for each pulse has the form given in eq. 3.38. The z-polarized pump pulse has the following properties: a resonant transition frequency at the Franck-Condon point has a value of

$52416\ 2\pi{\cdot}c{\cdot}cm^{-1}$, a pulse duration of $t_p = 25$ fs and a field amplitude of $E_0 = 8.0$ GV/m which corresponds to an average field intensity of $I \approx 1.07 \times 10^{13}$ W/cm^2. The optimized dump pulse has the following properties: is x-polarized, has a transition frequency of $\omega = 21730\ 2\pi{\cdot}c{\cdot}cm^{-1}$, a pulse duration of $t_p = 10$ fs and a field amplitude of $E_0 = 8.0$ GV/m ($I \approx 1.07 \times 10^{13}$ W/cm^2).

The delay time between the pump and the dump pulses is exploited in order to control the dynamics on the unbound a^1E state. The essential time steps, used in quantifying the extent of control, are defined in fig. 6.13. The initial time of the simulation is defined as $t_0 = 0$ fs, $n\Delta t$ describes time at the nth time step, the time delay t_{delay}, is the time at which the dump pulse is initiated, and t_f is the final time step. The angle of dissociation, given in eq. 6.7, is rewritten below as

$$\alpha = \arctan\left(\frac{\langle y_{\text{Co}-\text{CO}}(t_f)\rangle - \langle y_{\text{Co}-\text{CO}}(t_{delay} + 1\Delta t)\rangle}{\langle x_{\text{Co}-\text{CH}_3}(t_f)\rangle - \langle x_{\text{Co}-\text{CH}_3}(t_{delay} + 1\Delta t)\rangle}\right), \qquad (6.8)$$

and accounts for the initial position of the wavepacket on the dissociative state, a^1E, rather than the position at the FC point. If the position of the wavepacket is always taken at the FC point, the angle becomes heavily dependent on the amount of time the wavepacket has to evolve, and therefore the angle of dissociation becomes a poor quantifier. If however, the initial position of the wavepacket is defined on the state on which it is dissociating, then the angle of dissociation, if the wavepacket moves in a straight line, is independent of the amount of time the wavepacket has to evolve. This becomes clearer when one considers the terms in eq. 6.8. The first term of the numerator defines the expectation value for the position of the center of the wavepacket at the final time (t_f) . The second term defines the expectation value for the position of the center of the wavepacket at the moment it is transferred to the a^1E state, specifically after the dump pulse has been initiated, ($t_{delay} + 1\Delta t$). The final time, t_f was chosen as $t_f = t_{delay} + 100$ fs, i.e. the wavepacket was allowed 100 fs to evolve on the unbound a^1E state.

Results and Analysis

Angle of Dissociation   A series of pump-dump simulations were performed on the ground a^1A_1, unbound a^1E and bound b^1A_1 electronic states. The pump pulse with a duration of 25 fs transferred population from the ground a^1A_1 to the excited b^1A_1. An ultrashort (10 fs) dump pulse transferred population from the excited b^1A_1 to the unbound a^1E electronic state. The onset of the dump pulse was controlled by the time delay, t_{delay}, which
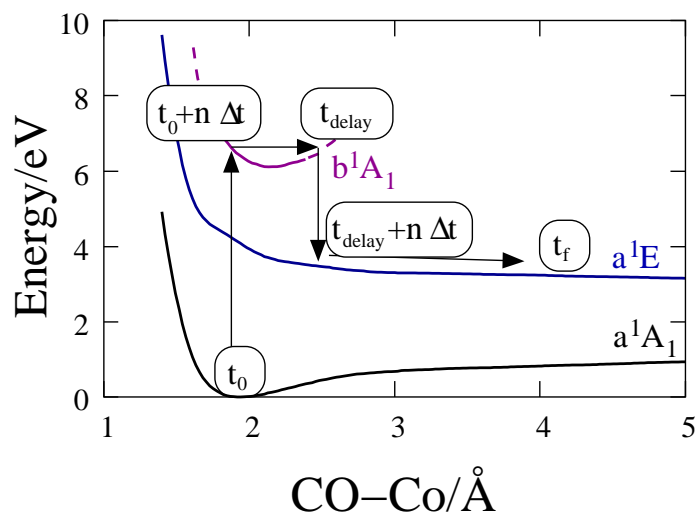
Figure 6.13: A one-dimensional cut of three electronic states used in the pump-dump control scheme depicting the essential time parameters: t_0 is the initial time of the simulation defined as zero, $n\Delta t$ describes the discretization of time as the nth time step, and the delay time, t_{delay} is the time at which the dump pulse is initiated, and t_f is the final time step.

was varied between 15 and 130 fs. The time of propagation always proceeded 100 fs after the dump pulse was extinguished, and the time step used was $\Delta t = 0.05$ fs. During each simulation the expectation value for the position of the center of mass of the wavepacket on the a^1E unbound state was measured at each time step. The angle of dissociation, α, was calculated according to eq. 6.8, and is plotted in fig. 6.14 against the delay time, t_{delay}. The maximum of the curve occurs at a delay time of $t_{delay} = 20$ fs, and corresponds to the maximum angle of dissociation achieved in favor of the carbonyl dissociation, $\alpha = 32.9°$. The minimum of the curve occurs at a delay time of $t_{delay} = 90$ fs, and corresponds to an angle of dissociation of $\alpha = -0.2°$. This indicates an exclusive dissociation of the methyl ligand from the cobalt. These values should be compared to the angle of dissociation of the natural wavepacket dynamics, namely $\alpha = 27.4°$. The exclusive breakage of the Co-CH_3 bond is obtained with an angle slightly less than $0°$. The negative angle is due to the transferred momentum of the wavepacket from the b^1A_1 state to the unbound a^1E state and the topography of the unbound state. This will be discussed in the following section. However, it should be emphasized that the cobalt-methyl bond is broken exclusively in this control method. The selective breakage of the CO ligand using this method of control is not exclusive, but the angle of dissociation was altered in its favor by $5.5°$, changing the rate at which the two bonds break.
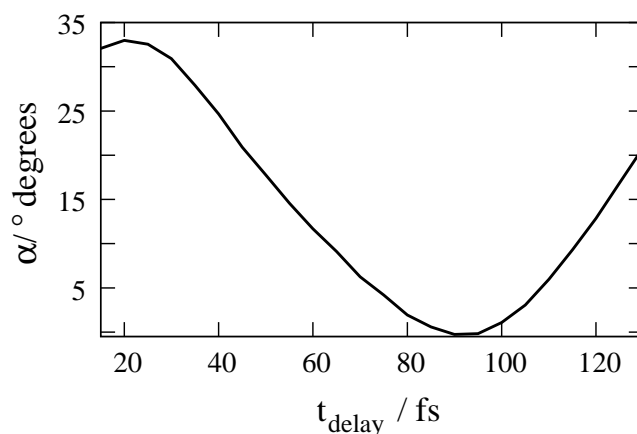
Figure 6.14: The dissociation angle α, in degrees, plotted against the delay time t_{delay}. The final time for each simulation is defined as $t_f = t_{delay} + 100$ fs, so that the wavepacket on the unbound a^1E state, regardless of the delay time, was allowed 100 fs to evolve. The maximum angle for the carbonyl dissociation, $\alpha = 32.9°$ is found at $t_{delay} = 22.5$ fs. The maximum angle for dissociation of the methyl ligand $\alpha = -0.2°$ is found at $t_{delay} = 90$ fs.

Control Analysis

Bond Length   Analysis of the bond elongations along each coordinate has been investigated for the three cases of dissociation on the unbound a^1E state: i) the natural dissociation starting at the FC point, ii) the maximum angle achieved towards CO dissociation, and iii) the minimum angle of the dissociation, corresponding to complete homolysis of CH_3. The position of the wavepacket was calculated at each time step of the propagation along the two coordinates corresponding to the stretching of the Co-CH_3 and the Co-CO bond, generalized as $\langle r_L \rangle$. The resulting elongations along both coordinates have been plotted for the three aforementioned cases in fig. 6.15, where the ligand being stretched is denoted by L. The bond length of the Co-CO bond is plotted as dotted lines and the solid lines depict the length of the Co-CH_3 bond. The two curves in fig. 6.15a, which begin at $t=0$, describe the natural elongation of the cobalt-ligand bonds upon vertical excitation, i.e. the position of the wavepacket starts at the equilibrium coordinates on the a^1E state. The metal-ligand bond being stretched is labeled as, L=CO and CH_3. An equal velocity of bond elongation, in which the curves in figs. 6.15 would run parallel, would lead to an angle of dissociation of 45°. The CO ligand increases its distance from the cobalt metal at a rate slower than that of the CH_3 ligand in all three cases of fig. 6.15, indicating an angle of dissociation less than 45°, see eq. 6.8. The set of curves in fig. 6.15b, has a similar behavior to those in fig. 6.15a. The initial position of the wavepacket on the a^1E state occurs
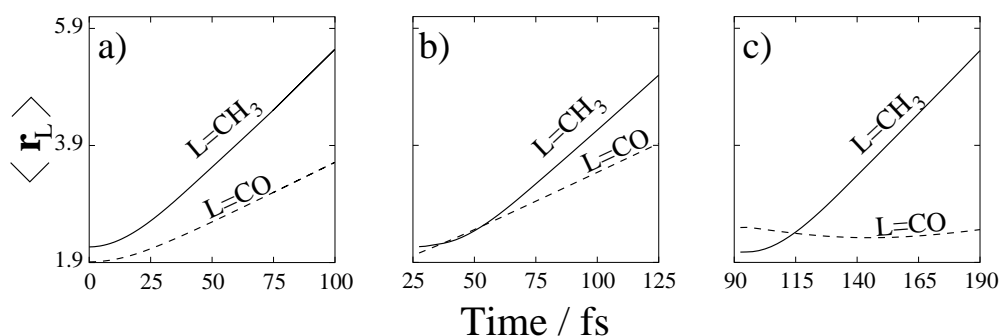
Figure 6.15: Bond elongations of the two ligands L= CH_3 and CO and corresponding to a) the dissociation of the wavepacket vertically excited from the Franck-Condon point (the natural dissociation), b) the dissociation occurring from a pump-dump mechanism which maximizes the angle of dissociation $\alpha = 32.9°$, and c) the dissociation occurring from a pump-dump mechanism that minimizes the angle of dissociation $\alpha = -0.2°$ leading to a single metal-ligand breakage of CH_3. The initial time of plots b) and c) correspond to the initiation of the dump pulse, i.e. b) 25 fs and c) 90 fs.

at a Co-CO elongation of 0.14 Å in comparison to the equilibrium position, compare with fig. 6.15a. The distance between the two curves after 100 fs is much smaller than that of the natural dissociation and corresponds to a change of 5.5° in the angle of dissociation. The curves in fig. 6.15c begin at a large Co-CO bond elongation of 0.57 Å and a small contraction, 0.08 Å, of the Co-CH_3 bond. Note that in the pump-dump type control experiments presented in the literature up-to-date, the elongation of the bond in the upper-most electronic state corresponds to the bond that is broken on the unbound electronic state, in this case would be the Co-CO bond; however, the quantum dynamics that occur on the unbound state here occur differently. Specifically, the bond that is elongated on the upper electronic state (Co-CH_3) is the bond that is not broken on the unbound state. This behavior is depicted in fig. 6.15c. The Co-CO bond length is elongated on the bound b^1A_1 state and begins its evolution on the unbound a^1E state at 90 fs with these values (cf. dotted lines of figs. 6.15a and 6.15b). The wavepacket evolution on the unbound state occurs such that the Co-CO bond no longer expands, but rather the Co-CH_3 bond. These temporal bond lengths are indicative of an exclusive Co-CH_3 bond breakage. Since the momentum of the wavepacket is conserved and plays an important role in the dynamics, the remainder of the discussion will incorporate the momentum of the wavepacket on the bound b^1A_1 state in order to elucidate the dynamics of the wavepacket on the unbound a^1E state.

Momentum   The expectation value of the momentum along each coordinate is calculated as

$$\langle \mathbf{p}_r \rangle = \langle \Psi_j(t) | \nabla_r | \Psi_j(t) \rangle \tag{6.9}$$

where $|\Psi_j(t)\rangle$ is the wavepacket evolving over time t on the electronic state j, and r represents the two coordinates q_1 (Co-CH$_3$) and q_2 (Co-CO). The momentum of the wavepacket from the natural dynamics on the upper b^1A_1 electronic state are investigated and plotted in fig. 6.16. The momentum along the q_2 coordinate is plotted in a dashed line and the momentum along the q_1 coordinate is plotted in a solid line. Upon a vertical excitation, the momentum in the q_1 coordinate, represented by the Co-CH$_3$ bond stretching, is hardly affected and remains fairly constant while the momentum of wavepacket in the q_2 coordinate, represented by the Co-CO bond stretching, increases consistently until it reaches a maximum at ~ 35.0 fs. The rate at which the Co-CO bond expands slows over the period between $t = 35$ and 80 fs. At $t = 80$ fs the wavepacket's momentum is zero and corresponds to the complete expansion of the Co-CO bond. The negative values of momentum beyond 80 fs describe the contraction of the Co-CO bond. The wavepacket's temporal momentum will be used to discuss the extent of control attained from the pump-dump mechanism applied in this work.
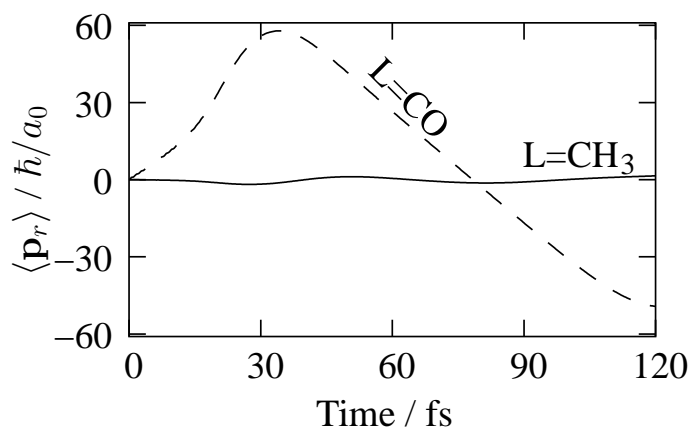

Figure 6.16: The expectation value for the wavepacket's momentum on the b^1A_1 electronic state upon a vertical transition is plotted from $t = 0$ fs to $t = 120$ fs. The momentum axis is r dependent and corresponds to either the q_1 (Co-CH$_3$) or q_2 (Co-CO) coordinate. The momentum along the q_1 coordinate is depicted by a solid line and labeled L=CH$_3$ and the momentum along the q_2 coordinate is depicted by a dashed line and labeled L=CO.

Maximum Increase of Dissociation Angle   The angle of dissociation defined in eq. 6.8 is maximized on the unbound a^1E state in order to change the rate of dissociation of the CH_3 and CO ligands. The natural angle of dissociation is $\alpha = 27.4°$ and the maximized value for the employed pump-dump mechanism is $\alpha = 32.9°$. This corresponds to an increase of $5.5°$ in the angle of dissociation. The pump pulse has a duration of $t_p = 25$ fs during which time population is transferred from the ground state a^1A_1 to the upper electronic state b^1A_1 via a single photon. The amplitude of 8 GV/m was used to ensure a substantial transfer of population. Due to the topography of the excited state potential energy surface, the wavepacket reaches its maximum momentum energy in the q_2 coordinate at $t \sim 35$ fs, while the momentum in the q_1 coordinate is nearly zero as indicated in fig. 6.16. If only the momentum of the wavepacket is considered, it would be advantageous to center the ultrashort dump pulse around the maximum momentum value in order maximize the angle of dissociation. However, during this time the Co-CO bond is expanding, and the Co-CH_3 bond is not. At larger Co-CO bond lengths, the topography of the potential surface favors the Co-CH_3 bond elongation. In other words, the force vectors due to the PES that the wavepacket feels at longer Co-CO bond lengths are oriented mostly in the q_1 coordinate and outweigh the momentum of the wavepacket. Only by considering both the momentum of the wavepacket and the topography of the PES can one understand the dynamics of the wavepacket. Therefore the best combination of the wavepacket's momentum and the position on the PES occurs at $t = 25$ fs when the dump pulse is turned on. The length of the dump pulse used was 10 fs and its duration was chosen as to induce a transition from the bound b^1A_1 to the unbound a^1E state within a time period in which the bond lengths have not varied greatly. The evolution of the wavepacket using this pump-dump mechanism is captured in snapshots at times $t = 0, 30, 50$ and 100 fs, and plotted for each of the three electronic states in fig. 6.17. The initial wavepacket was taken as the ground vibrational wave function of the ground electronic state. The second snapshot is taken at $t = 30$ fs and corresponds to the time when the dump pulse has reached its maximum amplitude. The wavepacket on the unbound a^1E state is located at the same position as the wavepacket on the bound b^1A_1 state. The next two snapshots occur at $t = 50$ and 100 fs. The wavepacket on the bound b^1A_1 state evolves along the Co-CO axis, while the wavepacket on the unbound a^1E state evolves at an angle corresponding to $\alpha = 32.9°$, and indicates the dissociation of both the ${}^\bullet CH_3$ and the CO ligand.

Maximum Decrease of Dissociation Angle   The angle of dissociation defined in eq. 6.8 has been minimized on the unbound a^1E state, producing the exclusive products: ${}^\bullet CH_3$
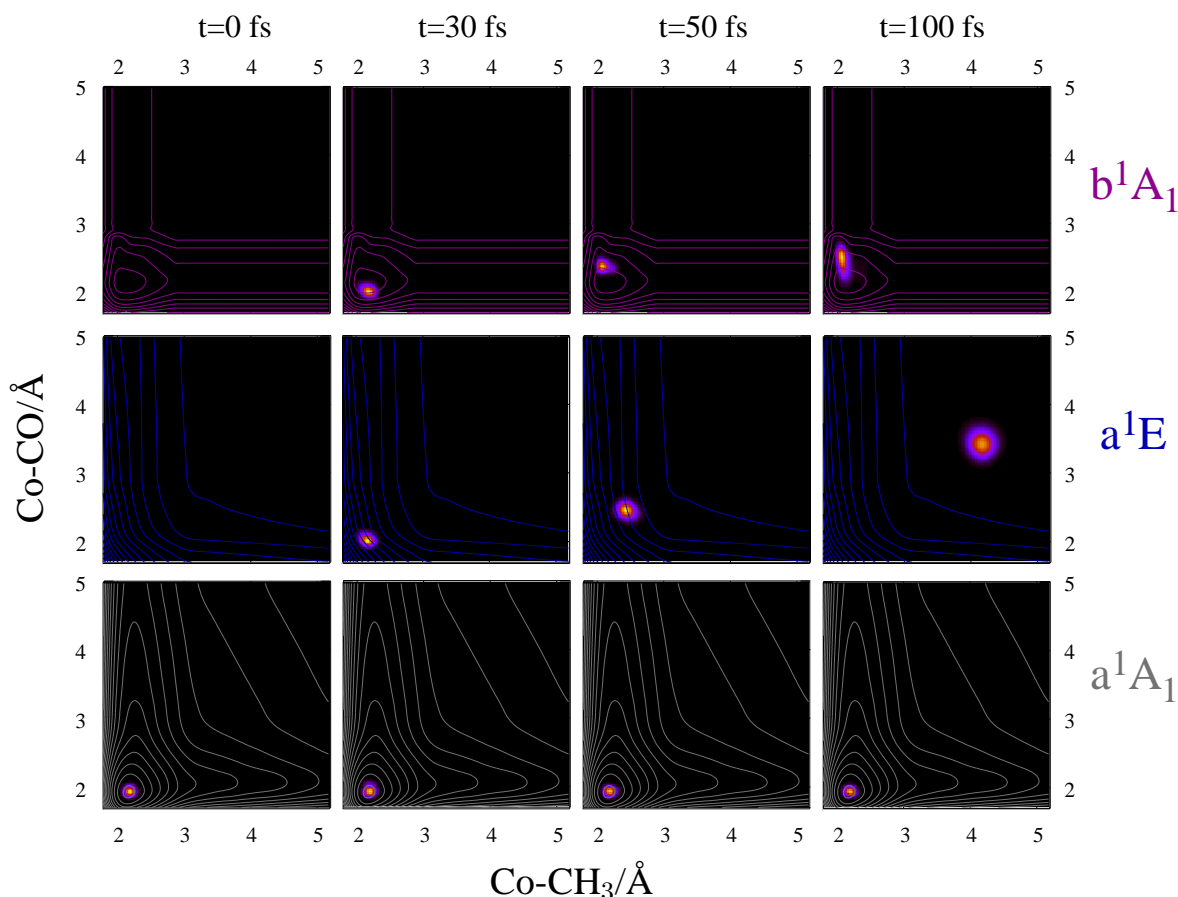
Figure 6.17: Snapshots of the wavepacket dynamics at $t = 30, 50$ and 100 fs, induced by a pump-dump mechanism. The transition $a^1A_1 \rightarrow b^1A_1$ occurs via the pump pulse whose duration is $t_p^{pump} = 25$ fs and the dump pulse initiated at $t_{delay} = 25$ fs with a pulse duration of $t_p^{dump} = 10$ fs induces the transition, $b^1A_1 \rightarrow a^1E$. The wavepacket in the upper a^1A_1 state is affected greatly by the surface and gains momentum in the Co-CO direction where the maximum momentum occurs at around $t = 35$ fs. The wavepacket is transferred in part to the a^1E unbound state between 25 and 35 fs. The wavepacket motion on the unbound state is indicative of a double bond breakage forming the following products: $^\bullet CH_3 + {}^\bullet Co(CO)_3 + CO$.

and $^\bullet Co(CO)_4$. The pump pulse with a duration of $t_p = 25$ fs transfers population from the ground state a^1A_1 to the upper electronic state b^1A_1 via a single photon. Due to the topography of bound state potential energy surface, the wavepacket reaches its maximum Co-CO bond extension at $t \sim 78$ fs. The Co-CO bond elongation reached is 0.57Å. At the same point in time, the Co-CH$_3$ bond has contracted 0.08Å. The exclusive Co-CH$_3$ bond breakage control mechanism is elucidated by examining the topography of the unbound a^1E PES as well as the momentum of the wavepacket on the bound b^1A_1 electronic state.
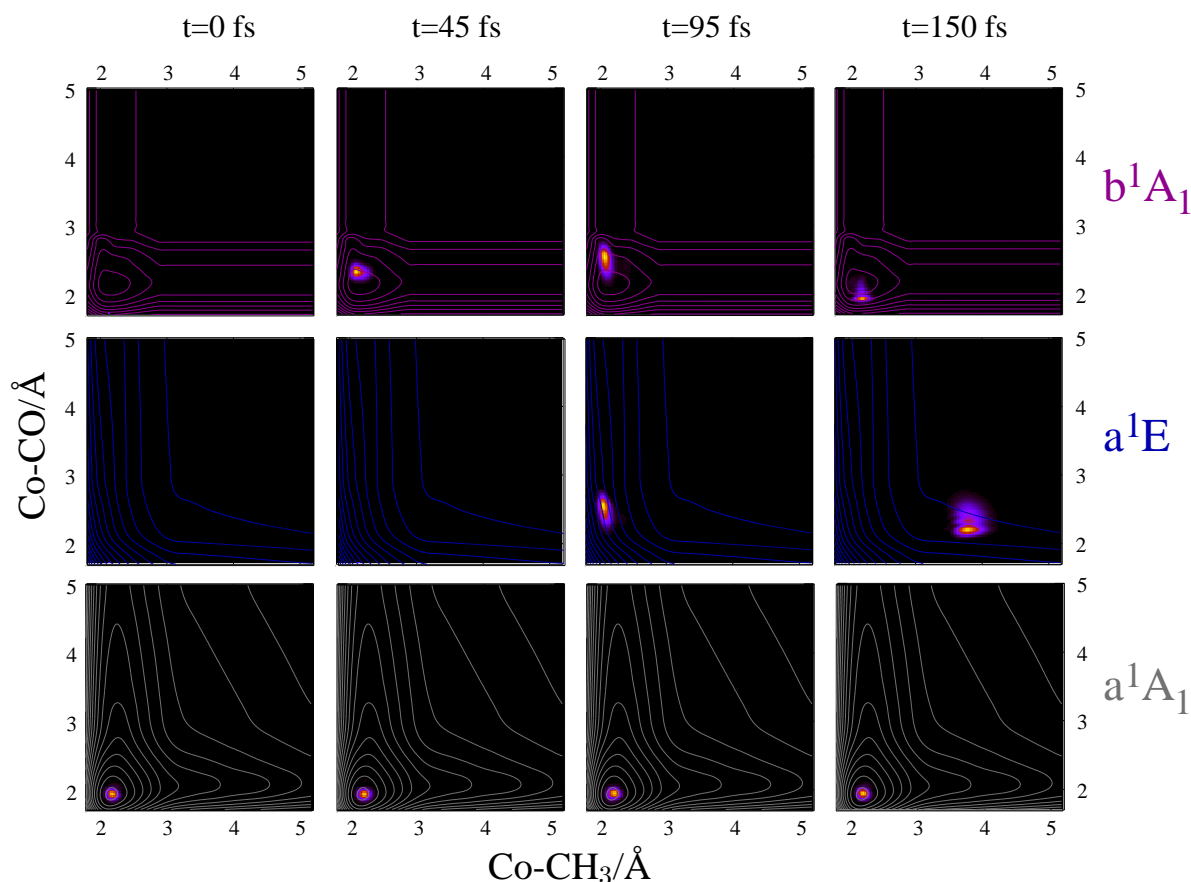
Figure 6.18: Snapshots of the wavepacket dynamics at $t = 45, 95$ and 150 fs, induced by a pump-dump mechanism. The transition $a^1A_1 \rightarrow b^1A_1$ occurs via the pump pulse whose duration is $t_p^{\text{pump}} = 25$ fs and the dump pulse initiated at $t_{delay} = 90$ fs with a pulse duration of $t_p^{\text{dump}} = 10$ fs induces the transition, $b^1A_1 \rightarrow a^1E$. The wavepacket in the upper a^1A_1 state moves along the Co-CO axis, at $t = 78$ fs the wavepacket has reached its turning point and begins its motion in the reverse direction. The wavepacket is transferred in part to the a^1E unbound state between 90 and 100 fs. The wavepacket motion on the unbound state is indicative of a dissociation of the molecule into the following radical products: $^\bullet CH_3 + {}^\bullet Co(CO)_4$.

The topography of the unbound PES lacks dissociation channels, therefore the Co-CO bond elongation of 0.57Å on the bound b^1A_1 represents a position on the unbound a^1E state that has its force vectors pointing in favor of the Co-CH$_3$ bond dissociation. If the wavepacket is influenced only by the topography of the unbound PES, then dissociation of the methyl ligand should occur nearly exclusively. However, as can be seen in fig. 6.14 the optimum angle of dissociation occurs at $t = 90$ and not at $t = 78$ fs. This is due to topography of the PES. In order to obtain the dissociation angle $\alpha = -0.2°$, a negative momentum along the Co-CO bond length is needed in order to counteract the

force inherent to the unbound surface. The optimized angle of dissociation is therefore achieved with a delay time, $t_{delay} = 90$ fs, rather than at $t = 78$ fs when the wavepacket's momentum in the Co-CO direction is zero. The evolution of the wavepacket is captured in snapshots at times $t = 0, 45, 95$ and 150 fs and is plotted for each of the three electronic states in fig. 6.18. The initial wavepacket ($t = 0$) was taken as the ground vibrational wave function of the ground electronic state. The second snapshot is taken at $t = 45$ fs and corresponds to a time of 20 fs after the termination of the pump pulse which had a duration of $t_p = 25$ fs. The wavepacket located on the bound b^1A_1 state has evolved to longer Co-CO bond lengths. The next snapshot occurs at $t = 95$ fs and corresponds to the maximum amplitude of the dump pulse which has a duration of $t_p = 10$ fs. The wavepacket on the b^1A_1 state has already reached its turning point and the Co-CO bond length contracts. The wavepacket on the unbound a^1E state has a negative momentum conserved from the vertical transfer from the bound b^1A_1 state and experiences a force inherent to the unbound PES which together elongate the Co-CH$_3$ bond. The final snapshot occurs at $t = 150$ fs and the wavepacket on the bound b^1A_1 state is contracted and is located near the FC point while the wavepacket on the unbound a^1E state evolves at an angle corresponding to $\alpha = -0.2°$, and depicts the exclusive single bond breakage which exclusively produces the following products, $^\bullet CH_3 + {}^\bullet Co(CO)_4$.

6.4   Nonresonant Multiphoton Transitions

It is the intent of this section to investigate the application of NMT to femtosecond quantum dynamical simulations, as well as its applicability with OCT. The numerical simulations have been carried out for the molecular system CpMn(CO)$_3$ (Cp=η^5-C$_5$H$_5$). This choice was motivated by recently reported closed–loop feedback experiments [27]. There, it has been shown that the yield of the parent ion CpMn(CO)$_3^+$ can be maximized with respect to that of its fragments (i.e. CpMn(CO)$_2^+$) under the influence of an ultrashort optimally shaped laser pulse.

The experimental setup used a transformed–limited laser pulse with a wavelength of 800 nm and a duration of 87 fs at full width half maximum (fwhm). The resulting optimal pulse [27] shows mainly two subpulses with durations of about 40 fs (fwhm) and wavelengths slightly blue chirped from 800 nm. According to highly correlated *ab initio* electronic structure calculations [27, 40] the optical transitions taking place within

the experimental optimal pulse are consistent with a nonresonant two-photon transition from the electronic ground state a^{1}A' to the neutral singlet c^{1}A' state, and a nonresonant three-photon transition from the c^{1}A' state to the b^{2}A' ionic state.

Quantum molecular dynamic and optimal control (OC) simulations developed within the context of NMT will be presented here on a reduced two-level electronic system of CpMn(CO)$_3$. The specific transition of interest is from the ground a^{1}A' to the excited electronic c^{1}A' state, see fig. 6.19. Simulations are performed on a one-dimensional grid representing the Mn-CO bond length and contains 512 points distributed between 1.2 and 15.0 Å. The following will first elucidate the application of NMT to solving the TDSE, and second will exemplify its use in OCT.

6.4.1   Solving the TDSE for NMT

Nonresonant Two-photon Transitions   The following simulations compare the temporal evolution of the population on the excited c^{1}A' state between nonresonant two-photon and the strongly off-resonant single-photon transitions.

Nonresonant two-photon transitions within the scope of RWA have been simulated. The kernel, $K_{ab}(t, \bar{t})$, appearing in eq. 5.45, assumed to be linearly expandable, is replaced by the nonresonant two-photon contribution of K_2, see eq. 5.38. The resulting equations of motion for the two level system have been derived on this basis and are given explicitly in eqs. 5.65 and 5.66. The laser pulse used in this study is described by eq. 5.6. A photon energy of $\hbar\omega = 1.715$ eV (wavelength of 723 nm) is applied which corresponds to half of the resonant transition frequency between the ground a^{1}A' and the electronically excited b^{1}A' state. The shape of the laser field is defined by eq. 5.7 and the pulse duration of $t_p = 100$ fs is used for each simulation. The field amplitude E_0 is varied three times with the values 15, 20 and 25 GV/m, as is denoted in fig. 6.20 which corresponde to the average field intensities of I$\approx 3.0 \times 10^{13}$ W/cm^2, 5.3×10^{13} W/cm^2, and 8.3×10^{13} W/cm^2, respectively. The effective two-photon coupling, $\mu_{ab}^{(2)}$, see eq. 5.56, characterizes a dipole moment from the primary state space to the secondary state space and vice-versa. Because this value is not easily calculable, the two-photon dipole matrix elements are modeled using the transition dipole moment at the FC point between these two states, $\mu_{\text{eff}} = 0.4\, ea_0$, and the mean density of secondary states, $\bar{\varrho} = 50$ eV^{-1}.
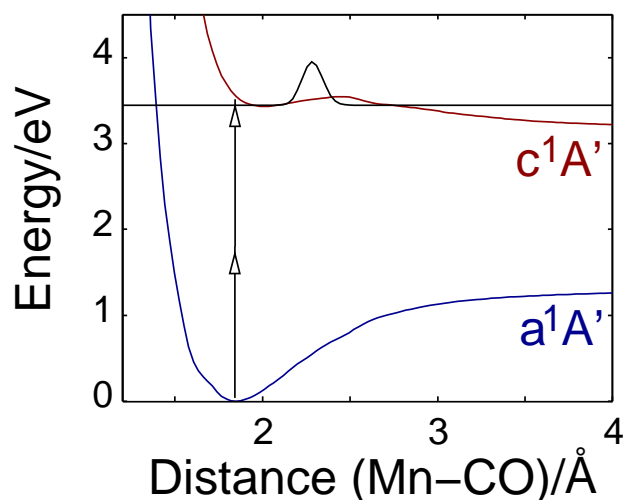
Figure 6.19: *Ab initio* potential energy curves of CpMn(CO)$_3$ along the Mn-CO bond length coordinate. The arrows indicate a nonresonant two-photon transition from the electronic ground state a^{1}A' to the electronic excited singlet state c^{1}A'. The black line displays the vibrational target state $|\chi_f^{(\mathrm{tar})}\rangle$ located near the right turning point on the weakly bound c^{1}A' state.

Calculations of the off-resonant single-photon transitions induced with the same laser parameters as the nonresonant two-photon transitions are performed for reference. The equations of motion for the single-photon transition are solved using eqs. 5.60 and 5.61. The off-resonant single-photon transition is characterized by a constant transition dipole function with the value at the FC point, $\mu_{fg} = 0.4\ ea_0$.

The temporal population of the c^{1}A' electronic state for the three aforementioned field strengths have been plotted in fig. 6.20 over 120 fs. The panel on the left captures the population accruing from the nonresonant two-photon transition. The strongest laser field (25 GV/m) induces a population transfer of $P_f(t_f) \sim 1.2 \times 10^{-2}$ from the a^{1}A' to the c^{1}A' state. The panel on the right captures the corresponding temporal population induced by a strongly off-resonant single-photon transition. The population builds up to a value $P_f\ (t = 50\ \mathrm{fs}) \sim 1.9 \times 10^{-2}$ and then dwindles to a residual population on the order of 10^{-9} for the three corresponding field strengths. The population that remains on the c^{1}A' electronic state for the nonresonant two-photon transition is seven orders of magnitude larger than that from the off-resonant one-photon transition.
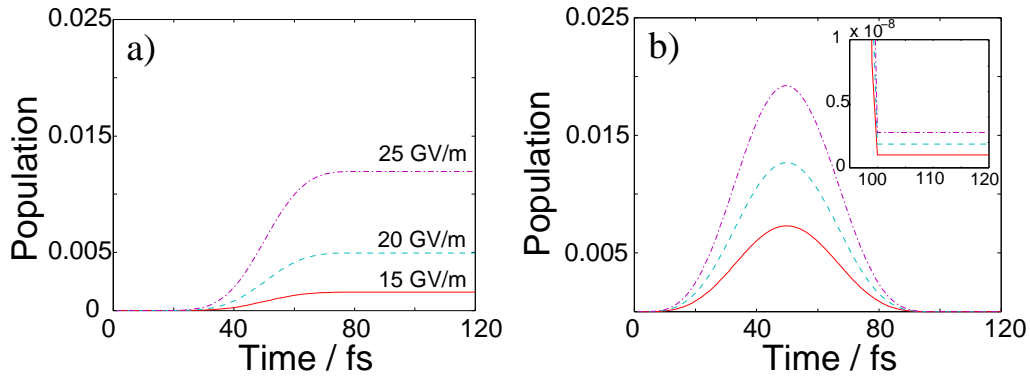
Figure 6.20: a) Nonresonant two-photon transitions in CpMn(CO)$_3$ compared with b) nonresonant single-photon transitions. Shown are the temporal evolutions of the excited state population $P_f(t)$ on the c^{1}A' excited electronic state. Excitation has been achieved by a pulse with photon energy $\hbar\omega = 1.715$ eV, envelope $\sin^2(\pi t/t_p)$, and duration of $t_p = 100$ fs. The effective two-photon coupling is characterized by $\mu_{\text{eff}} = 0.4$ a.u. and $\bar{\varrho} = 50$ eV^{-1} and the single-photon transitions by $\mu_{fg} = 0.4$ a.u. The maximum field strength has been varied from 15 to 25 GV/m. The insert in b) enlarges the population achieved by single-photon excitation upon termination of the pulse.

Nonresonant Three-photon Transitions   The following simulations are intended to compare the temporal evolution of the population on the excited c^{1}A' state, between nonresonant three-photon and the strongly off-resonant single-photon transitions.

Nonresonant three-photon transitions within the scope of RWA have been simulated. The kernel, $K_{ab}(t, \bar{t})$, appearing in eq. 5.45, assumed to be linearly expandable, is replaced by the nonresonant three-photon contribution of K_3, see eq. 5.39. The resulting equations of motion for the two-level system have been derived on this basis and are given explicitly in eqs. 5.69 and 5.70. The laser pulse used in this study is described by eq. 5.6. A photon energy of $\hbar\omega = 1.143$ eV, wavelength of 1034 nm, is applied and corresponds to a third of the resonant transition frequency between the ground a^{1}A' and the electronic excited c^{1}A' state. The shape of the laser field is defined by eq. 5.7 and the pulse duration for each simulation is $t_p = 100$ fs. As in the case of 2-photon transitions, the field amplitude E_0 is varied three times with the values 15, 20 and 25 GV/m, as is denoted in fig. 6.21. The effective three-photon coupling, $\mu_{ab}^{(3)}$, see eq. 5.59, is again approximated by $\mu_{\text{eff}} = 0.4$ a.u. A mean density of secondary states of $\bar{\varrho} = 50$ eV^{-1} is used.

Calculations of the off-resonant single-photon transitions induced with the same laser parameters as the nonresonant three-photon transitions are performed. The equations of motion for the single-photon transition are solved using eqs. 5.60 and 5.61. The off-
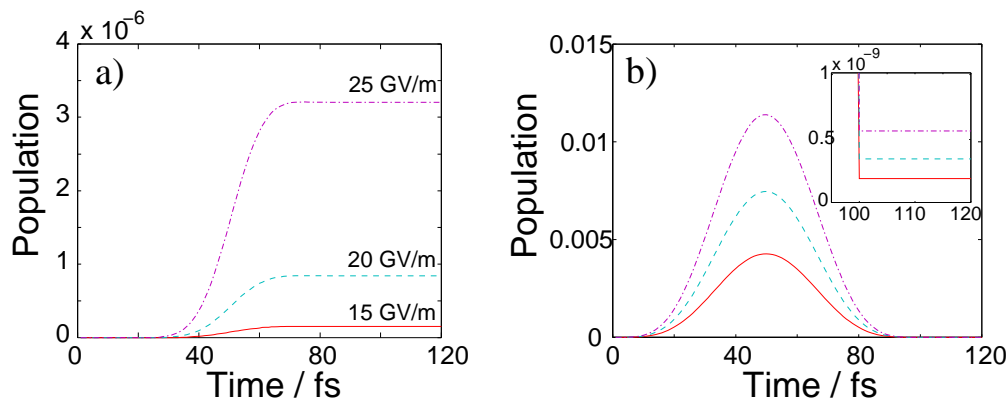
Figure 6.21: a) Nonresonant three-photon transitions in CpMn(CO)$_3$ compared with b) nonresonant single-photon transitions. Shown are the temporal evolutions of the excited state population $P_f(t)$ on the c^{1}A' excited electronic state. Excitation has been achieved by applying a pulse with photon energy $\hbar\omega = 1.143$ eV, envelope $\sin^2(\pi t/t_p)$, and duration of $t_p = 100$ fs. The effective three-photon coupling is characterized by $\mu_{\text{eff}} = 0.4$ a.u. and $\bar{\varrho} = 50$ eV^{-1} and the single-photon transitions by $\mu_{fg} = 0.4$ a.u. The maximum field strength has been varied from 15 to 25 GV/m. The insert in b) enlarges the population which has been achieved by a single-photon transition upon termination of the pulse.

resonant single-photon transition is characterized by a constant transition dipole function at the FC point, $\mu_{fg} = 0.4$ ea_0.

The temporal population on the c^{1}A' electronic state for the three aforementioned field strengths have been plotted in fig. 6.21 over 120 fs. The panel a) captures the population accruing from the nonresonant three-photon transitions with a photon energy of $\hbar\omega = 1.143$ eV. The strongest laser field (25 GV/m) induces a population transfer of $P_f(t_f) \sim 3.2 \times 10^{-6}$ from the a^{1}A' to the c^{1}A' state. The panel b) captures the corresponding temporal population induced by a strongly off-resonant single-photon transitions. The population builds up to a value of P_f ($t = 50$ fs) $\sim 1.2 \times 10^{-2}$ and then dwindles to a residual population on the order of 10^{-10}. The population that remains on the c^{1}A' electronic state for the nonresonant three-photon transition is now only four orders of magnitude larger than that from the off-resonant one-photon transition, in comparison to the seven orders of magnitude in the two-photon nonresonant transition investigation.

The comparison between the nonresonant two- and three-photon transitions with the off-resonant single photon transitions indicates that the contribution to the population of the latter at the end of the laser pulse are much smaller in magnitude than the nonresonant

transitions. Although the population that occurs from the off-resonant single-photon transitions does reach a higher population at half the pulse duration, the other half of the laser depopulates the state. Lastly, the population that accrues from the nonresonant two-photon transitions is much larger in magnitude than that for the nonresonant three-photon transitions, as is expected.

Population Dependence on Effective Coupling Matrix Elements   The effective coupling matrix elements, $\mu_{ab}^{(2)}$ and $\mu_{ab}^{(3)}$, couple the primary states with the secondary states and are not easily calculable. Therefore they are approximated here using eqs. 5.56 and 5.59 by applying the mean value of the density of secondary states $\bar{\varrho}$ and the effective (mean) dipole matrix elements μ_{eff} between the primary and secondary states. These values are varied to analyze their influence on the population of the excited c^1A' state. The laser pulse used is given by eq. 5.6 with the squared sinus shape function, eq. 5.7. The field amplitude was held constant at $E_0 = 10$ GV/m with a pulse duration of $t_p = 200$ fs. The photon energies of $\hbar\omega = 1.715$ and 1.143 eV were used for the nonresonant two-photon and three-photon transitions, respectively. The influence of varying the values μ_{eff} and $\bar{\varrho}$ in the effective coupling matrix elements on the excited state population P_f while holding the other parameters constant can be visualized in fig. 6.22.

The population for the nonresonant two-photon transitions has a quadratic behavior when considering a constant effective dipole and varying the density of states. Likewise, the behavior for the nonresonant three-photon transitions is cubic. The transition population increases as both variables are increased. This is expected since increasing the transition dipole moment in resonant single-photon transitions also increases the population. Increasing the density of secondary states supports off-resonant transitions and will increase the overall population.

6.4.2   OCT Applied to NMT

Optimal control theory has been developed in section 5.5 for nonresonant multiphoton transitions under the rotating wave approximation. The OCT iteration scheme described in section 4.2, was programmed in the context of NMT and RWA using Matlab7 programming language [152]. The results that follow are intended to demonstrate the applicability of the theory and have been obtained by employing the two-level a^1A', c^1A'
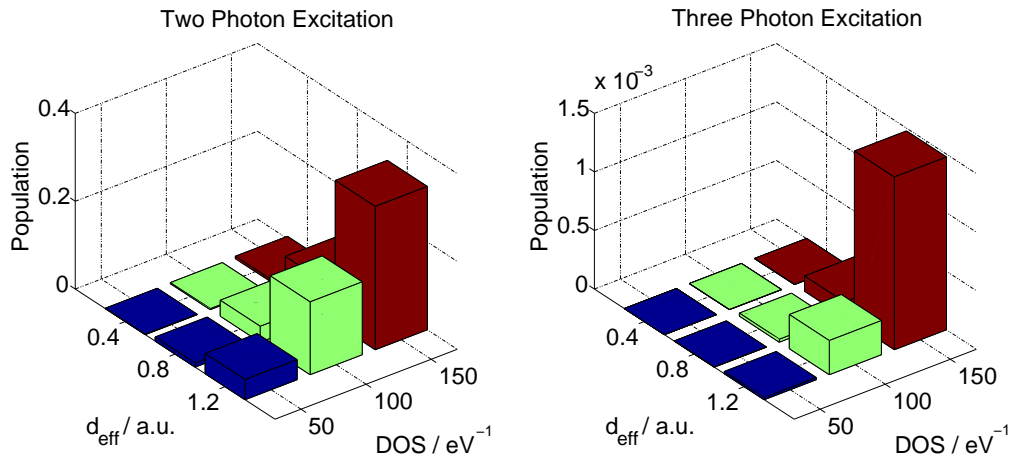
Figure 6.22: Excited state population P_e in CpMn(CO)$_3$ on the c^{1}A' excited electronic state after two-photon transitions (left panel) and three-photon transitions (right panel). The parameters μ_{eff} and the DOS $\bar{\varrho}$ entering the two-photon as well as three-photon coupling matrix elements are varied. Excitation has been achieved by applying pulses with a photon energy $\hbar\omega$ of 1.715 eV for the two-photon transition and of 1.143 eV for the three-photon transitions. The field amplitude equals 10 GV/m (I$\approx$ 1.3 $\times$ 10$^{13}W/cm^2$), the field envelope is $\sin^2(\pi t/t_p)$, and the duration $t_p = 200$ fs for both cases.

electronic system of CpMn(CO)$_3$. Optimal control simulations have been explored for three cases: i) resonant single-photon transitions, ii) nonresonant two-photon transitions, and iii) nonresonant three-photon transitions.

The results of this section will be divided into two studies. The first study (I) will compare the three optimal control fields obtained from OC simulations for each of the three case; i, ii, and iii, in which the control yield $\mathcal{Q}$ is maintained by altering the penalty factor λ. The second study (II) examines how the penalty factor λ as well as the position of the target state affect the control yield for case ii, in which only the nonresonant two-photon transitions are considered, and should behave similarly for case iii, when considering nonresonant three-photon transitions.

Computational Details

In the following studies, the initial pulse for each simulation is described by eq. 5.6 where the shape function $s(t)$ is given by eq. 5.7 and the pulse duration is $t_p = 100$ fs. The initial field strength was taken as $E_0 = 10$ GV/m and each simulation took place

over a time period of $t_f = 120$ fs. The calculated control field was not restricted to the initial pulse duration of $t_p = 100$ fs but if necessary could incorporate the extra 20 fs to achieve its task. The initial wave function was taken as the ground vibrational wave function located in the ground electronic state, $|\chi_{g0}\rangle$. The target vibrational wavepacket $|\chi_f^{(\text{tar})}\rangle$ is represented in fig. 6.19 on the c^{1}A' electronic state, for study I. The position of the target state was chosen based on the deciphered mechanism for the feedback-loop control mechanism, in which excitation from this position produces the parent ion versus the daughter ion. The position of the target vibrational wavepacket is varied in study II and will be explicitly given.

Study I: A Comparison between Resonant and Nonresonant OCT

Simulations have been performed for a resonant single-photon transition, and nonresonant two- and three-photon transitions. The penalty function λ was varied in order to achieve similar control yields $\mathcal{Q} \sim 50\%$ for each simulation. The results for each case are described below explicitly based on the results depicted in fig. 6.23.

Case i: Resonant One-photon Transitions   The control task pictured in panel a1) of fig. 6.23 was achieved by solving the equations of motion for a resonant single-photon transition, given by eqs. 5.60 and 5.61, using the aforementioned laser pulse parameters with a photon energy of $\hbar\omega = 3.430$ eV, and a dipole value of $\mu_{fg} = 0.4\ ea_0$. The iterative scheme described in section 4.2 is applied. The results obtained from solving the control task are depicted in panels b1), c1), and d1) of fig. 6.23. Specifically panel b1) presents the control yield $\mathcal{Q}$ (solid curve) and renormalized control yield q (dotted curve), see eqns. 4.2 and 5.77 respectively. The control yield $\mathcal{Q} \sim 50\%$ displays a convergence within 10 iterative steps. The percentage of the total population on the c^{1}A' state that has reached the position of the target state is given by the renormalized yield, calculated here as $q \sim 69\%$. The temporal evolution of the population $P_g(t)$ on the ground a^{1}A' state (dotted curve) and the population $P_f(t)$ on the c^{1}A' electronic state (solid curve), and the norm conservation (horizontal line) are presented in panel c1). The maximum population reached on the c^{1}A' electronic state is $P_f(t_f) \sim 72\%$. In panel d1) the optimized control field that maximizes the overlap between the ground state vibrational wave function $|\chi_g(t_0)\rangle$ and the target state wave function $|\chi_f^{(\text{tar})}\rangle$ is shown, under the influence of the penalty factor λ, and derived from the complex optimal field, see eq. 5.85. The optimized control field is deduced from

eq. 5.6 as $\mathbf{n}\mathbf{E}(t) = \mathrm{Re}[E(t)\exp(i\omega t)]$ by insertion of the complex valued optimal field envelope. The resulting calculated field shows a distinct asymmetry with a field strength of $E_0 \sim 2.5$ GV/m.

Case ii: Nonresonant Two-photon Transitions   The control task for a nonresonant two-photon transition is depicted in panel a2) of fig. 6.23. The task is achieved by solving the equations of motion for nonresonant two-photon transitions given by eqs. 5.65 and 5.66, where $\mu_{gg} = \mu_{ff} = 0$, using the aforementioned laser pulse parameters with a photon energy of $\hbar\omega = 1.175$ eV. The effective two-photon coupling matrix element $\mu_{fg}^{(2)}$, defined in eq. 5.56, is approximated by the effective transition dipole moment, $\mu_{\mathrm{eff}} = 0.4\ ea_0$, and by the mean density of secondary states $\bar{\varrho} = 50$ eV^{-1}, and the control field is calculated based on eq. 5.90. The results obtained from solving the control task are depicted in panels b2), c2) and d2) of fig. 6.23. The control yield $\mathcal{Q}$ (solid curve) and renormalized control yield q (dotted curve) are represented in panel b2). The control yield $\mathcal{Q} \sim 50\%$ converges again within 10 iterative steps. The percentage of the total population on the c^{1}A' state that reaches the position of the target state is given by the renormalized yield, calculated here as $q \sim 69\%$. Panel c2) shows the temporal evolution of the population $P_g(t)$ on the ground a^{1}A' state (dotted curve) and the population $P_f(t)$ on the c^{1}A' electronic state (solid curve), and also the norm conservation (horizontal line). The maximum population reached on the c^{1}A' electronic state is $P_f(t_f) \sim 72\%$. The optimized control field that maximizes the ground state vibrational wave function $|\chi_g(t_0)\rangle$ with that of the target state wave function $|\chi_f^{(\mathrm{tar})}\rangle$ is presented in panel d2). The field is calculated according to eq. 5.6 and the envelope $E(t)$ is deduced from $\mathcal{E}(t) = |\mathcal{E}(t)|\exp(i\varphi(t))$ as $E(t) = \sqrt{|\mathcal{E}(t)|}\exp(i\varphi(t)/2)$. The resulting calculated field shows a distinct asymmetry and has a field strength of $E_0 \sim 60$ GV/m which can be considered in the strong-field regime. It should be noted that strong-field phenomena have not yet been incorporated into our model, so that our results should only be taken as a reference of the applicability of the developed theory. Results obtained with less intense fields can be found in the study II.

Case iii: Nonresonant Three-photon Transitions   The OC simulation for nonresonant three-photon transitions has been carried out. The control task along with the results are depicted in panel a3) in fig. 6.23. The control task is achieved by solving the equations of motion for a nonresonant three-photon transition, given by eqs. 5.69 and 5.70, using the
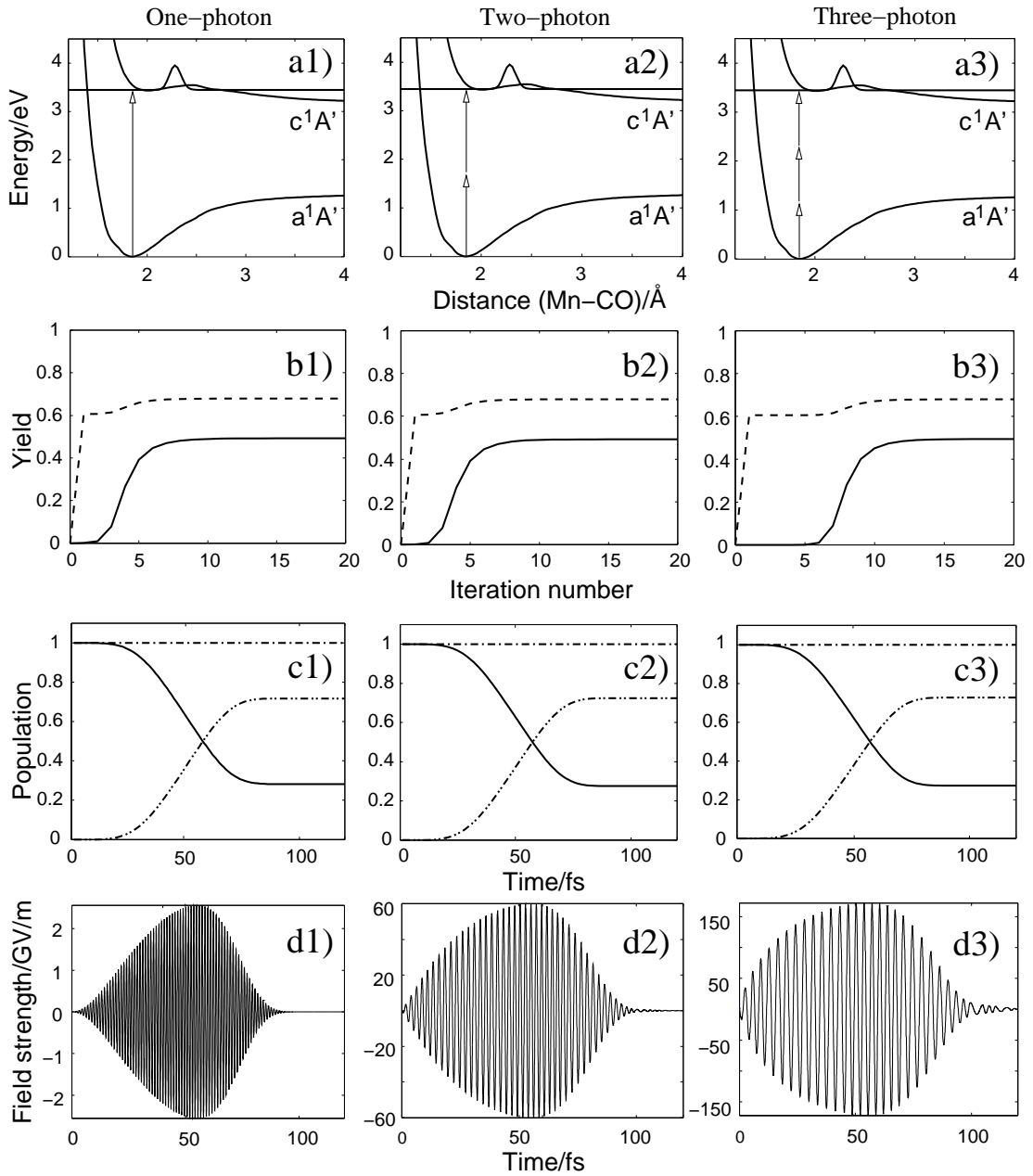
Figure 6.23: Laser pulse control in CpMn(CO)$_3$ for resonant single-photon and nonresonant two- and three-photon transitions into the excited c^{1}A' electronic state where the target vibrational wavepacket $|\chi_f^{(\mathrm{tar})}\rangle$ is positioned near the right turning point. The photon energy referring to the carrier wave is 3.430, 1.715, and 1.143 eV respectively. The final time of the control task equals $t_f = 120$ fs. The field amplitude of the pulse which initiates the iterative solution of the OCT is $E_0 = 10$ GV/m. The dipole moment for the single-photon transition is characterized by $\mu_{fg} = 0.4\, ea_0$, and the effective two- and three-photon coupling is characterized by $\mu_{\mathrm{eff}} = 0.4\, ea_0$ and $\bar{\varrho} = 50$ eV^{-1}. Each control task is represented column-wise by its control yield ($\mathcal{Q}$ = solid line) and renormalized control yield (q = dashed line), the temporal population of the ground state (P_g =solid line) and of the excited state (P_f = dashed–dotted line), as well as the temporal evolution of the optimal pulse. The penalty factors, $\lambda = 7.42 \times 10^{-5}$ fs^{-1}(GV/m)$^{-2}$, 7.40×10^{-11} fs^{-1}(GV/m)$^{-4}$, and 5.59×10^{-17} fs^{-1}(GV/m)$^{-6}$ were adjusted to obtain similar control yields.

same laser pulse parameters as with the previous two simulations, now with a photon energy of $\hbar\omega = 1.143$ eV. The effective three-photon coupling matrix element $\mu_{fg}^{(3)}$, defined in eq. 5.59, is approximated by the effective transition dipole moment, $\mu_{\text{eff}} = 0.4 \, ea_0$, and by the mean density of secondary states $\bar{\varrho} = 50$ eV^{-1}. The electric field driving the wavepacket evolution is given in eq. 5.94. The results that resulted from the control task are depicted in panels b3), c3), and d3) of fig. 6.23. The control yield $\mathcal{Q}$ (solid curve) and renormalized control yield q (dotted curve) are presented in panel b3). The control yield $\mathcal{Q} \sim 50\%$, for nonresonant three-photon transitions, converges within 15 iterative steps. The percentage of the total population on the c^{1}A' state that has reached the position of the target state is given by the renormalized yield, calculated here as $q \sim 69\%$. Panel c3) captures the temporal evolution of the population $P_g(t)$ on the ground a^{1}A' state (dotted curve) and the population $P_f(t)$ on the c^{1}A' electronic state (solid curve), along with the norm conservation (horizontal line). The maximum population reached on the c^{1}A' electronic state is $P_f(t_f) \sim 72\%$. The final panel d3) presents the optimized control field that maximizes the overlap of the ground state vibrational wave function $|\chi_g(t_0)\rangle$ to the target state function $|\chi_f^{(\text{tar})}\rangle$. It has been calculated according to eq. 5.6 with the envelope $E(t)$ deduced from $\mathcal{E}(t) = |\mathcal{E}(t)| \exp(i\varphi(t))$ as $E(t) = \sqrt[3]{|\mathcal{E}(t)|} \exp(i\varphi(t)/3)$. The resulting calculated control field is broader than the single- and two-photon analogues, has a field strength of $E_0 \sim 165$ GV/m (I$\approx 3.6 \times 10^{15} W/cm^2$), now in the strong-field regime. As in the previous case, these pulses should be only considered as an exemplification of the theory, since the strong-field regime phenomena are not implemented in this model.

Study II: Varying Penalty Factors and Vibrational Target States

The penalty factor λ and the target wavepacket $|\chi^{(\text{tar})}\rangle$ on the c^{1}A' state are systematically varied to obtain a quantitative picture of their effects on the control yield and the renormalized control yield. The variations of these parameters will only be studied in case ii (for the nonresonant two-photon transitions), though the effects should be extendable to the nonresonant three-photon transitions. This section is divided up into two studies. Case iia) analyzes the effect of changing the penalty factor on the strength of the optimal control fields, which are typically in the strong-field regime, and case iib) the position of the vibrational target state will be varied and the penalty factor will be set as to produce experimentally accessible field strengths.

Study IIa: Strong Field Reference Calculations   The calculated control field depends directly on the penalty factor λ. This study will investigate the effect the penalty function has on the control field, control yield $\mathcal{Q}$, eq. 4.2, and the renormalized control yield q, eq. 5.77, for nonresonant two-photon transitions. These results are presented in table 6.7.

As expected, an increase of λ leads to a decrease of the field strength. Those pulses which result in a rather large control yield $\mathcal{Q}$ need optimal pulses with a remarkably large field strength. Such strong pulses are beyond the employed theory of the two electronic state model, they demonstrate, nevertheless, the successful combination of OCT and NMT processes. Besides $\mathcal{Q}$, table 6.7 also displays the renormalized control yield q. Since the target state can be reached in very direct manner, q is largely independent of the overall pulse intensity. Thus, the portion of the wave function put into the excited state matches the target state with a high probability.

Table 6.7: The yield $\mathcal{Q}$, the renormalized yield q, and the maximum $E_{\max}$ of the field strength (in GV/m) for different used penalty factors λ (in 10^{-10} fs^{-1} (GV/m)$^{-4}$) of the described control scheme

$\mathcal{Q}$	q	$E_{\max}$	λ
0.68	0.82	58.1	3.0
0.29	0.74	42.2	5.9
0.0049	0.72	14.7	23.6
0.0009	0.72	9.6	46.2

Study IIb: Experimentally Accessible Pulse Intensities   Based on the previous results, it is intended to solve the control task for different target vibrational wavepackets, in which the field strength remains below the strong field limit of I$\approx 10^{14}$-10^{15} W/cm^2, by setting the penalty factor λ accordingly. This is done exemplarily for nonresonant two-photon transitions and is straightforward for the nonresonant three-photon transitions.

Table 6.8 presents the results for four control tasks, in which the position of the target vibrational wavepacket is systematically shifted from internuclear distances of 2.12 to 2.28Å. The first two positions of 2.12 and 2.17Å lie before the right turning point of the c^{1}A' electronic state, located at 2.23Å, and the last point is beyond the turning point at a distance of 2.28 Å. With this study we intend to demonstrate the applicability of OCT with NMT for a general target.

In all cases it was possible to find reasonable penalty factors λ that lead to optimized control fields in the TW/cm^2 regime as well as to substantial renormalized yields q. This indicates that the proposed optimal control approach transfers population on the order of

Table 6.8: The target state, defined at different inter-nuclear distances (in Å) where the target wave function has its maximum; the yield $\mathcal{Q}(10^{-3})$; the renormalized yield q; and maximum $E_{\max}$ of the field strength (GV/m), for different used penalty factors λ (10^{-10} fs^{-1} (GV/m)$^{-4}$).

Target	$\mathcal{Q}$	q	$E_{\max}$	λ
2.12	5.20	0.74	15.6	18.3
2.17	4.85	0.76	14.7	23.6
2.23	3.31	0.72	13.4	27.7
2.28	1.00	0.61	10.3	25.2

parts per million when accounting for two-photon processes and that it is not particular to a specific target state.

In summary, within this work we show that nonresonant multiphoton transitions have been successfully implemented into femtosecond spectroscopy. Its use in OCT has also been exemplified by its application to nonresonant two- and three-photon transitions within the $CpMn(CO)_3$ two-level model system. For multiphoton transitions, obtained control fields tend to be in the strong-field regime; however, by changing the penalty factor, one can reduce the control field intensity that consequently reduces the control yield. Nevertheless, the presented renormalized control yield, which indicates the amount of the driven wavepacket that has reached the position of the predefined target state, is above 60%, demonstrating the applicability of the here proposed method.